A critical look at interpretation of electrochemical impedance spectra of sol-gel coated aluminium

K.A. Yasakau , M. Starykevich , M.G.S. Ferreira , M.L. Zheludkevich

PII: S0013-4686(21)00381-9
DOI: https://doi.org/10.1016/j.electacta.2021.138091
Reference: EA 138091

To appear in: *Electrochimica Acta*

Received date: 17 December 2020
Revised date: 13 February 2021
Accepted date: 3 March 2021

Please cite this article as: K.A. Yasakau , M. Starykevich , M.G.S. Ferreira , M.L. Zheludkevich , A critical look at interpretation of electrochemical impedance spectra of sol-gel coated aluminium, *Electrochimica Acta* (2021), doi: https://doi.org/10.1016/j.electacta.2021.138091

Highlights

- Model anodised aluminium samples were coated with sol-gel and characterized by EIS
- The contribution of various interface phenomena to the EIS spectra was discussed
- The barrier oxide film was always visible as a time constant on the EIS spectra
- Degradation of the sol-gel/oxide interface was assessed via oxide capacitance

A critical look at interpretation of electrochemical impedance spectra of sol-gel coated aluminium

K.A. Yasakau[1*], M. Starykevich[1], M.G.S. Ferreira[1], M.L. Zheludkevich[2,3].

[1]Department of Materials and Ceramic Engineering, CICECO - Aveiro institute of materials, University of Aveiro, 3810-193 Aveiro, Portugal.

[2] MagIC – Magnesium Innovation Centre, Institute of Materials Research Helmholtz-Zentrum Geesthacht, Max-Planck Str. 1, 21502 Geesthacht, Germany.

[3]Institute for Materials Science, Faculty of Engineering, Kiel University, 24143 Kiel, Germany

Abstract

A proper assignment of time constants is important for the correct interpretation of the electrochemical impedance spectra of coated substrates. In this work several model aluminium samples with different anodic oxide thicknesses were prepared and characterised. The aluminium samples were coated by a hybrid sol-gel formulation and studied by electrochemical impedance spectroscopy (EIS) during immersion in NaCl solution. A hierarchical model containing three R-C elements adequately described the impedance spectra of the coated samples. The R-C elements described the properties of sol-gel coatings, aluminium oxide layers and corrosion process. The contribution of the aluminium oxide layer to impedance was unambiguously proven to be at middle frequencies on the spectra. Furthermore, the "real" capacitances of oxide layers were obtained from two capacitance–CPE equations and their applicability was scrutinized. The obtained results presented an opportunity to determine the adhesion behaviour of the sol-gel coatings to the oxide layers, which was studied by analysing the ratio of the oxide layer capacitance of the sol-gel coated samples to the capacitance of the uncoated one. It was demonstrated that the exposed surface area of the oxide to the electrolyte was about 60-68 % and was not changing during immersion. Based on these findings, a degradation model of the sol-gel coating on anodised aluminium was proposed.

Keywords: Aluminium oxide, Electrochemical impedance spectroscopy, anodising, sol-gel, corrosion.

[*] Corresponding author: K.A. Yasakau, Department of Materials and Ceramic Engineering, CICECO - Aveiro institute of materials, University of Aveiro, 3810-193 Aveiro, Portugal, *E-mail address:* kyasakau@ua.pt

Introduction

Aluminium alloys became important structural materials in the automotive, aerospace and marine industries. In general aluminium alloys possess advantages in terms of mechanical properties, oxidation resistance, weight to strength ratio and fabrication cost over other materials [1]. Aluminium alloys, in particular copper-containing ones, are highly susceptibility to corrosion especially in the chloride-based environment due to the presence of an abundant amount of intermetallics which lead to local micro-galvanic corrosion [2-4] and other forms of corrosion like filiform [5, 6] and intergranular corrosion [7, 8]. Therefore, protective coatings are typically applied to decrease corrosion degradation and increase the service life of alloys.

State of the art corrosion protection system contains several layers [9] such as pre-treatment that provides improved adhesion to the metal surface and some active corrosion protection; primer that normally incorporates inhibitive pigments and improves corrosion protection of metal; and topcoat that improves mechanical properties of the protection system. One of the important areas of research was finding effective and environmentally acceptable alternatives to substitute the use of toxic chromates in the industry [9-12]. Many efforts have been devoted to development and studying the performance of different coatings for corrosion protection of aluminium alloys [13, 14].Various inorganic anodic, conversion coatings and hybrid organic-inorganic layers have been actively studied as possible pre-treatments for aluminium alloys [13, 15-21]. Sol-gel coatings, contrastingly to other pre-treatments, form strong chemical bonds with metals, oxides and organic primers [18, 22] and have good corrosion performance [23]. Moreover, the sol-gel matrix is often used as a storage of inhibitors and different nanocontainers [24-27].

Corrosion performance of coatings is typically evaluated via standard accelerated corrosion tests like neutral salt spray tests or cyclic climate tests [28, 29]. Although such tests are effective, they do not explain the mechanisms of corrosion and do not reveal the degradation kinetics of coatings. Electrochemical impedance spectroscopy (EIS), on the other hand, is a useful tool for studying corrosion resistance of coated metals and follow the evolution of coatings properties, water uptake and development of corrosion activity during immersion [30-35]. EIS was successfully applied in conjunction with accelerated testing including a combination of DC and AC measurements (AC/DC/AC) [36, 37], and to understand the kinetics of cathodic disbondment of organic coatings [38]. In literature, however, there is a large discrepancy of results concerning the interpretation of the impedance spectra of coated aluminium alloys by organic and hybrid coatings. EIS was employed to better understand properties of the coatings that were submitted to accelerated corrosion exposure [39]. The coatings exposed to corrosive electrolytes display non ideal capacitive behaviour and resistivity distribution resulting in constant phase element (CPE) behaviour, which called for development of various models that describe the EIS spectra of the coatings [40-42].

Classical equivalent circuit models based on combination of time constants [35, 43] are typically employed for fitting EIS spectra of sol-gel coated metals [44, 45]. The high frequency part of the impedance spectrum of the coated metal is related to the barrier properties of the coating, while the low frequency segment reflects the corrosion activity on the metal surface

[34]. However, such properties are not the only ones that can be studied by the EIS method. For example, the EIS spectra of the coated aluminium alloys often show the response of another property which is related to the presence of an intermediate layer between the metal and coating [26, 46, 47]. Such response can be attributed to the dielectric properties of the aluminium oxide film, which is naturally formed in air [48, 49] or after chemical etching treatment that is usually applied during the alloy preparation steps [24, 50]. Time constants found in the low and middle frequency region of spectra of coated aluminium alloy substrates can be erroneously assigned to organic layers or corrosion processes [51, 52]. The middle frequency time constant has been also assigned to the interfacial layer in sol-gel coatings [53]. And the existence of the aluminium oxide film is often neglected. By monitoring the evolution of EIS fitting parameters during corrosion testing it is possible to study the active corrosion protective capabilities [36, 54, 55], adhesive properties of the coatings and the electrochemically active area of the coated samples [56-58]. The latter works demonstrated the possibility to determine degradation of the metal coating interface by studying the evolution of pore resistance of the coating, double layer capacitance and charge transfer resistance. However, the properties of the oxide films on aluminium alloys were not extensively studied as possible means for evaluation of delamination and degradation of coatings. Moreover, since oxide films are often modelled by a circuit containing a CPE element, it requires finding effective capacitance expressed in F/cm^2 by using different equations developed by Hsu and Mansfeld [59], Brug et al. [60] and understand their applicability [61].

In this work model experiments were designed to study the physical characteristics of the sol-gel coated substrates and assess the degradation mechanism of the sol-gel/oxide interface during immersion. Aluminium oxide films having different thicknesses were grown on aluminium using a two-step anodising process in ammonium pentaborate electrolyte. Model hybrid sol-gels were applied on aluminium samples forming dense and uniform coatings. These coatings were studied by electrochemical impedance spectroscopy during immersion in NaCl electrolyte. The obtained impedance spectra were fitted with equivalent circuit models and fitting parameters corresponding to oxide films were scrutinized.

Experimental

Materials and sample preparation

Aluminium 99 wt.% having impurities content of Cu <1000, Fe <7000, Mn <1000, Si <5000, Zn <1000 (ppm) and higly pure aluminium 99.999 wt.%, having impurities content about Cu~0.3, Fe~0.3, Mg~1.2, Si~0.8 (ppm), were acquired from Goodfellow. Rectangular coupons (5x3.5 cm) were cleaned in acetone and absolute ethanol in an ultrasonic bath for 10 min at each cleaning step. Electrochemical polishing has been performed to reduce the surface roughness and remove the top layer of aluminium. The polishing solution contained perchloric acid and absolute ethanol in a volume ratio (1:5). An Agilent DC current source N5751A was used in a potentiostatic mode by applying 20 V between the aluminium sample and the titanium foil counter electrode. The solution was kept at temperature of 3 °C using a water circulating thermostat system and was constantly stirred during the polishing step to avoid local overheating. The polished samples were rinsed with absolute ethanol, dried in a flow of air and stored in a desiccator.

Anodising

Aluminium anodising was performed in 0.1 M ammonium pentaborate electrolyte prepared using de-ionized water and AR grade ammonium pentaborate reagent (CAS 12046-03-6, Sigma Aldrich), at 20±1 °C. The two-step anodising procedure used was similar to that described elsewhere [62]. Samples were galvanostatically polarized at a current density of 1 mA/cm^2 using a Keithley 237High Voltage Source-Measure Unit. After the desired terminal voltage was achieved, the process was switched to a potentiostatic regime. In this step a constant voltage was applied. The procedure was carried out with the terminal voltages of 10, 20 and 40 V, producing the samples Al10, Al20 and Al40 respectively. The sample which has not been anodised is called Al0V for consistency reasons. Immediately after anodising the samples were rinsed with deionized water and dried in airflow. After the anodising step the samples were stored in a desiccator before use. For calibration of oxide thickness model anodic films were grown on high purity aluminium (99.999 wt.%).

Sol-gel synthesis and coating application

Sol-gel formulation #1 was based on a combination of Zirconium (IV) propoxide (CAS 23519-77-9 Sigma Aldrich) in Ethylacetoacetate (CAS 141-97-9, Fluka) and 3-glycidoxypropyltrimethoxysilane (CAS 2530-83-8 Sigma Aldrich) mixed with isopropanol (CAS 67630 Sigma Aldrich) which were preliminary hydrolyzed by addition of a diluted nitric acid solution and then mixed to form the final sol-gel formulation. The molar ratio between the Zr inorganic precursor and Si organic precursor was 1:5. Hybrid sol-gels have been produced following the sol-gel synthesis procedure described elsewhere [26].

Aluminium samples have been coated with the sol-gel using a dip-coating process. The samples were held in a sol-gel solution for 1 minute and then withdrawn at a rate of 18 cm/min. After dip coating the samples were dried in air for half an hour and then transferred to an oven heated up to 120 °C and cured during 80 min. The following samples have been prepared: electro-polished aluminium coated with the sol-gel formulation #1 (SG1Al0V), aluminium

anodised at 10V, 20V and 40V coated with the sol-gel formulation #1 SG1Al10V, SG1Al20V and SG1Al40V respectively.

Experimental techniques

Electrochemical Impedance Spectroscopy (EIS) was employed as the main technique for understanding the electrochemical response of the anodised aluminium and sol-gel coated aluminium samples during immersion. The measurements were performed using Gamry FAS2 Femtostat with a PCI4 controller. A conventional three-electrode cell setup was used, which comprised a saturated calomel reference electrode (SCE), a platinum foil as a counter electrode and the uncoated or coated aluminium samples as working electrodes. The measurements were carried out at a temperature of 22±1 ºC in a Faraday cage. The impedance measurements were performed in 0.5 M NaCl solution (prepared with Millipore™ water and 99.5 wt. % NaCl) at open circuit potential with an applied 10 mV RMS sinusoidal perturbation in the frequency range of 2.6×10^{-3}-1×10^{5} Hz with 7 data points per decade. The impedance plots were fitted using commercially available Echem Analyst (Gamry Inc.) software. Typically, three uncoated aluminium samples were measured for each condition, and the EIS measurements were performed in duplicate for sol-gel coated samples to check the reproducibility.

Atomic Force Microscopy (AFM). A Pico LE AFM equipped with PicoScan 2100 controller was employed to study the topography of aluminium samples before and after anodising. Topography studies were made in air using the semi-contact mode and highly doped Si probes with the radius of curvature less than 10 nm.

Glow discharge optical emission spectroscopy (GDOES) depth profile analysis of coatings was conducted with a HORIBA GD-Profiler 2. Radiofrequency plasma discharge with 40 W input power was ignited between the sample and a 4 mm copper anode at 650 Pa argon operating pressure. The plasma discharge etched the sample surface and optical emission spectra of the elements from the coating were obtained during the etching process. Three measurements were taken for each sample.

Hitachi S-4100 field emission scanning electron microscope (SEM) equipped with Rontec energy dispersive X-ray (EDX) spectrometer and a Hitachi SU-70 UHR Schottky Analytical FE-SEM coupled with a SDD-Bruker Quantax 400 EDS detector, operating at 25 and 15 kV correspondingly, were used to study the samples microstructure and the composition.

Results and discussion

1. Surface and depth profiles analyses of anodised aluminium

Figure 1 presents the AFM topography of aluminium samples before and after the anodising process. The surface was not significantly changed after the anodising when compared to electropolished one. AFM images show relatively flat surface having RMS roughness in the range of 1.1-1.3 nm for 0V, 10V and 20V samples and around 0.5 nm for 40V sample. At such a

small roughness the surface area difference between the geometrical and real surface can be considered as not significant.

Next, the anodised aluminium substrates were analysed by GDOES to determine the average oxide thickness. Preliminary, a calibration of GDOES profiles was performed on model anodic films with a known thickness grown on high purity aluminium (99.999 wt.%) (Figure 2). The anodised samples at 20 V and 40 V had the thickness about 28 nm and 56 nm respectively. The calculated etching rate was 2.5 nm/s. Afterwards, the oxide thickness of the anodised aluminium (99 wt.%) samples was calculated from the GDOES profiles and presented in Table 1. With increasing the anodising voltage the thickness increased, though thickness to voltage ratio decreased and was lower than the theoretical thickness (1.4 nm/V) [48]. Probably this effect can be attributed to the presence of some impurities in the aluminium matrix which may adversely affect the growth of the oxide film during anodising.

Having obtained the thickness of oxide films the anodised aluminium samples were characterized by electrochemical impedance spectroscopy during immersion in 0.1 M ammonium pentaborate solution at pH 7. This electrolyte was used to avoid possible destruction or modification of the oxide films which could happen in a corrosive electrolyte. Bode plots of aluminium before and after anodic film growth are presented in Figure 3. The spectra present only one clearly defined time constant attributed to the dielectric oxide layer (Figure 3). The increase of impedance modulus in the middle frequency range is seen when increasing anodising voltage (Figure 3). Such an increase is associated with thicker aluminium oxide films produced at higher anodising voltages. The spectra of anodised samples were fitted using an equivalent circuit (EC) with only one time constant which is associated with the dielectric properties of the anodic oxide film, (CPE_{oxide}) connected in parallel with the resistance of the oxide layer R_{ox} (Figure 3 inset). CPE elements were used instead of pure capacitors to account for the dispersion of properties of the dielectric layers at the sample surface. The oxide layer resistance here is not the electronic resistance but the resistance of the electrolyte in the minor defects and pores which are present in the oxide.

The obtained fitting parameters of CPE elements were used to calculate the "real" sol-gel or oxide capacitance. This was done using two types of capacitance-CPE relations assuming normal and surface distributions of time constants [61]. The distribution occurs when properties of the oxide layer (e.g. which are explored in this work) are changing giving a time constant dispersion. These properties can vary normal to the metal surface and along the metal surface. The "real" capacitance of an oxide layer that assumes the normal distribution of time constants was calculated using equation (1) taken from Hirschorn et al. [61], equivalent to the equation proposed by Hsu and Mansfeld [59, 61]:

$$C_{eff} = Q^{1/n} R_f^{(1-n)/n} \quad (1)$$

where C_{eff} is the oxide capacitance expressed in (F/cm^2), Q and n are CPE parameters and R_f is the film resistance. The effective capacitance that assumes the surface distribution of time constants in the presence of an Ohmic resistance can be expressed as [60, 61]:

$$C_{eff} = Q^{1/n}\left(\frac{R_e R_f}{R_e + R_f}\right)^{(1-n)/n} \quad (2)$$

where R_e is the global Ohmic resistance and R_f, Q, and $n_ć$ represent global properties of the oxide. The estimated oxide layer thicknesses using the equations (1) and (3), assuming the dielectric constant $\varepsilon_r = 9$, are close to the experimentally obtained oxide thickness values for anodised samples (Table 1). It should be noted that equation (2) does not seem to be applicable for calculation of the effective capacitance of the anodised layers. The calculated oxide thickness values using equation (3) are much higher than the experimentally obtained thicknesses of the anodic oxides (Figure 2). This conclusion is similar to the one made by Hirschorn et al. who employed equation (2) in the calculation of the effective capacitance of Nb_2O_5 films formed on Nb electrodes [61].

The effective relative dielectric constant of the oxide films can be estimated (Table 1) by inserting the calculated real capacitance of the oxide films, and the oxide thickness obtained from GDOES measurements into a plate capacitor relationship:

$$C = \varepsilon_0 \varepsilon_r A/d \quad (3)$$

where ε_0 represents the dielectric constant of vacuum ($8.8543\ 10^{-12}$ F/m), ε_r is the relative dielectric constant of the anodic oxide, *A* is the area of the electrode, and *d* is the thickness of the oxide layer. The reported values of ε_r for anodised Al_2O_3 vary between 7.5 and 15 [63-68]. In this work the dielectric constant for the native oxide film formed on aluminium after electropolishing procedure was assumed to be 9 (Table 2). Since the native oxide film had a very small thickness, GDOES measurements could not unambiguously determine the real oxide thickness. Therefore, the oxide film thickness of the electropolished sample (Al0V) was estimated from EIS spectra as about 2.1 nm ($\varepsilon_r = 9$). The properties of the rest of the samples were determined by calculating the capacitance from EIS measurements and the thickness obtained from GDOES measurements. The calculated capacitance values and relative dielectric constants of the various oxides are presented in Table 2. It appears that the dielectric constants are higher for the anodised samples Al10V, Al20V and Al40V with values about 9.2, 9.6 and 10 respectively. Oxide films measured by GDOES on anodised high pure Al (99.999 wt.%) (Figure 2) reveal higher thickness than on anodised Al (99 wt.%) (Table 2). Probably in the latter case the impurities in Al matrix affected the growth and properties of anodised samples. The impurities were found to affect the growth of oxide films on the aluminium [69, 70]. Oxide films produced in neutral electrolytes such as the ammonium pentaborate at the anodising voltages used in this work should be amorphous and oxide crystallinity appears only at higher anodising voltages [67]. Nevertheless, the values of relative dielectric constants are within the range reported in the literature [63-70].

2. Depth profile characterisation of the sol-gel coated anodised aluminium

The obtained capacitance and thickness information of the anodised samples will be used as the input data for the comparison between the uncoated aluminium samples and sol-gel coated

ones. Figure 4a presents a representative cross-section image of a pure aluminium sample coated by a sol-gel film. The sol-gel coating is dense and uniformly spread along the metal surface. The coating surface (not shown) is clear and without visible defects and cracks as was shown previously [26]. The thickness of the sol-gel layer estimated from cross-sections is around 2.2 µm. Sol-gel coatings deposited on anodised aluminium substrates show similar coating thickness as observed on GDOES profiles of one of the major element (Zr) of the sol-gel coating (Figure 4b). The profiles display the decrease of concentration of Zr element as one of the main components of the sol-gel matrix during etching of the coated samples in plasma discharge and the intersection between the profiles of Zr and Al is considered to be the thickness of sol-gel coatings.

3. Electrochemical characterization of sol-gel coated anodised aluminium during immersion

Sol-gel coated samples were immersed in 0.5 M NaCl solution during approximately 4 weeks. Bode plots of different samples not anodised and anodised at 10, 20 and 40 V are presented in Figure 5. Impedance spectra of uncoated samples are presented for comparison on each graph. Bode plots of the coated samples clearly show two relaxation processes. The capacitance at lower frequencies is close to that of the sample without sol-gel. This is observed for all the cases with different thickness of the oxide layers. These facts can unambiguously prove that the middle frequency time constant is associated with the oxide layer present on the surface. The relaxation process observed on the sol-gel coated samples at higher frequencies appears only after application of the hybrid film and is related to the response of its capacity and pore resistance. This suggestion agrees well with the previous studies reported in the literature [18, 26, 33, 71]. During a long immersion time the pore resistance of the sol-gel layer decreases which is seen on all the spectra (Figure 5). However, the impedance part associated with the oxide layer does not change significantly. Impedance spectra show a third time constant located at the very low frequencies. This time constant is typically attributed to the electrochemical corrosion processes at the metal surface [72]. All spectra revealed corrosion activity in all sol-gel coated samples during immersion.

Two standard equivalent circuit (EC) models presented in Figure 6 were used for fitting the EIS spectra. Such models are typically used to describe EIS spectra of sol-gel and organic coatings on metallic substrates [33-35]. In principle, different EC models representing RC connecting in series or hierarchical (cascade or ladder) models can be applied to fit EIS data of coated metallic samples and it is important to decide which of the models is applicable for the physical description of the system [35, 43]. Typically, sol-gel coatings have interlinked hybrid matrix which contains poorly polymerized regions. The latter become defects and pathways for the electrolyte to penetrate towards the oxide layer and metal [33]. The models were based on a combination of R-C elements that describe sol-gel and oxide dielectric films and interface phenomena at the metal/electrolyte and arranged in series or cascade. The CPE element was employed instead of capacitance in all the fitting procedures to account for the inhomogeneity of dielectric layers and dispersive character of time constants. Although EIS spectra do not clearly show the uncompensated electrolyte resistance (R_{sol}), it was a necessary element to improve the

fitting goodness. The following groups of elements were used in the EC models. The first R-C element was attributed to the sol-gel coating resistance (R_{coat}) and capacitance (CPE_{coat}). Next, the model included the second R-C element that characterizes the aluminium oxide film porosity (R_{ox}) and dielectric properties (CPE_{ox}). The third R-C element was used to account for the corrosion process that develops during immersion in the corrosive electrolyte. The corrosion process was characterized by the charge transfer resistance (R_{ct}) and double layer capacitance (CPE_{dl}). Macroscopic observations revealed a few small pits formed on the surface after immersion (not shown) thus this justifies the addition of R_{ct} and CPE_{dl} elements to the equivalent circuit model. Visual observations of the fit lines on the EIS spectra (Figure 5) revealed that the selected EC models (Figure 6) provide adequate fitting of the spectra.

Table 3 presents the numerical fitting values obtained for the samples after 1 day and 23 days immersion using the EC model in Figure 6b. The goodness of fits (Chi^2) was around 2-5×10^{-4} and reflected a good convergence between the experiment and fitting. During immersion the capacitance of the sol-gel coating (CPE_{coat}) increased, and the coating resistance (R_{coat}) decreased due to hydrolytic instability of the sol-gel coating in aggressive solutions, water absorption and active corrosion processes. On the other hand, the dielectric properties of oxide sub-layers (CPE_{ox}) were roughly similar during immersion (Table 3). The oxide layer resistance (R_{ox}) dropped during immersion because of local corrosion attack. The corrosion process manifested on the impedance spectra in the low-frequency part, though numerical fitting values showed relatively high resistance (R_{ct}) and low capacitance (CPE_{dl}) during immersion. It is acceptable to evaluate the dielectric properties of sol-gel coatings and oxide films by following the changes in CPE values. However, CPE parameters may be misleading because they do not represent real capacitance. Therefore, the properties of sol-gel coatings and oxide layers should be further examined by applying the capacitance–CPE relations (equations 1, 2).

3.1 Properties of the sol-gel coatings

Although there is some discrepancy between the CPE_{coat} values (nS s^{-a} cm^{-2}) presented in Table 3, to understand changes of the dielectric properties, the effective capacitance values expressed as (F/cm^2) should be used. Figure 7a presents the evolution of effective capacitance of the sol-gel coatings ($C_{coat\ eff}$) calculated using equation (1) versus square root of time ($t^{0.5}$). The capacitance values show similar values for the four different samples (Figure 7a). Since the coatings were produced using the same sol-gel formulation and procedure, it is expected that the calculated capacitance should be very similar for all sol-gel coatings. Dielectric properties of a sol-gel coating must be studied using direct measurements of the coating thickness and EIS data during immersion. By using equation 3 a relative dielectric constant of the sol-gel coating can be calculated knowing the experimentally obtained thickness (about 2.2 μm). The calculated dielectric constant is about 15-16, and such values are close to the values obtained for the inorganic zirconia-based sol-gel coatings [73]. During the initial period of immersion (about 1 day) the capacitance rapidly changes. Such changes may be explained by rapid water uptake [33]. At longer immersion time the slope on the capacitance – $t^{0.5}$ graph became smaller compared to the initial period of immersion (Figure 7a). During this period the sol-gel coating

could be affected by both hydrolytic degradation and water uptake. Assuming that the water transport follows the Fick's law the amount of water uptake in the coatings can be calculated according to the Brasher-Kingsbury's equation [74]:

$$\Phi_w = \frac{\log(\frac{C_t}{C_0})}{\log(\varepsilon_w)} \times 100\% \quad (4)$$

where Φ_w is the volume fraction of water in organic polymers, C_t is the coating capacitance at immersion time t, C_0 is the initial capacitance of dry coating and ε_w is the dielectric constant of water (80). Figure 7b shows the evolution of the water uptake plotted against the square root of time. There are two linear regions on the graph, which describe what seems to be two different kinetics of water uptake. The first region can be associated with the direct water uptake and is similar to the initial stage of water uptake of sol-gel coatings described elsewhere [51]. While the second one is most likely associated with the changes in the sol-gel matrix as was pointed earlier. This assumption was made because the water absorption process was not finite in a relatively thin sol-gel coating.

Consequently, the calculation of C_{eff} was also performed using equation (2). Figure 7c presents the evolution of effective capacitance. The graph displays a very high dispersion of the values especially at the later stage of immersion compared with the results presented in Figure 7a. Since the sol-gel coatings were similar, it is rational to say that the coatings do not show the behaviour that assumes the distribution over the surface of time constants, thus the equation 2 should not be applicable for calculation of the effective capacitance. Besides, the obtained R_{coat} values during immersion demonstrate a quite similar decrease during immersion, which is associated with the development of pores and cracks in the sol-gel coating matrix (Figure 7d). Next, we discuss the implications of the equations (1) and (2) in the calculation of the properties of the oxide films.

3.2 Properties of oxide layers

The evolution of the oxide layer resistance (R_{ox}) during immersion was plotted in Figure 8. The Figure displays a high scattering of the values especially for the samples having thicker anodic oxide layers. Such a lack of consistency in the values may be due to the fact that the EIS spectra are not finite, which means that the resistive part is poorly defined in the fitting (Figure 5). Nonetheless, the samples having thicker oxide layers reveal higher oxide resistance. Moreover, the resistance stays approximately at the same level during immersion demonstrating the stability of the oxide layer against corrosion attack.

Then, the oxide film capacitance data (CPE_{ox}) extracted from EIS fittings using the EC circuit (Figure 6b) was evaluated. The effective oxide layer capacitance (C_{eff}) was calculated using equations (1) and (2). Afterwards, the effective barrier oxide thickness was calculated using the capacitor formula (3) and relative dielectric permittivity values presented in Table 2. The calculation was performed under the assumption that the surface area of the oxide is equal to the geometric surface area of the sample. Figure 9 presents the evolution of the oxide thickness

calculated assuming the normal and surface distributions of time constants during immersion in NaCl solution. There are several important observations to be made. The oxide thickness values of the sample (Sg1Al0V) display a higher discrepancy compared with anodised samples that present very similar values (Figure 9). Therefore, there is a noticeable difference in calculating thickness using the real capacitance estimated from equations (1) and (2) especially for thin oxide films. Unlike for sol-gel coatings, oxide thickness did not significantly change for all the studied samples during immersion. This is justified by the fact that the used aluminium was relatively pure and the corrosive electrolyte had pH close to neutral, and in principle should not have led to the dissolution of the oxide [75]. However, the calculated oxide thickness of the coated substrates appears to be larger than that for the anodised samples only (Figure 9). The larger thickness may be explained in terms of partial coverage of the oxide surface by the sol-gel coating that effectively blocks the electrolyte contact with the oxide. Thus, the lower surface area of the exposed oxide to the solution gives a smaller capacitance value and, consequently, a higher calculated thickness.

4. Discussion

4.1. Applicability of EC models for fitting EIS spectra of sol-gel coated samples

Although the EC model employed for fitting produced adequate goodness of fitting and consistent parameters of the coating and oxide, a more thorough discussion is required to understand if other ECs are applicable for EIS fitting. As was pointed out by Amirudin and Thierry, the EC models having the same parameters but arranged differently can yield the same impedance [35]. Figure 10 presents two possible models for EIS spectra fitting of the coated metal. The first model (a) is a standard model that was used for EIS fitting of sol-gel coated samples. This model emulates pores in the coating which allow the contact with the oxide film. Only part of the oxide film has a connection to the electrolyte through pores, while the other part becomes inaccessible for the electrolyte due to chemical bonding between the coating and the oxide layer. However, attention has to be paid to the fact that the bonding of silane molecules to the surface is not ideal and leaves patches of the surface without silane bonding to the surface [22, 76] (Figure 10c). This happens because the sol-gel has high condensation degree with a large fraction of T2 and T3 siloxane species and presence of organic groups in the formulation which cause steric hindrance [77]. Due to the presence of a few pores in the oxide, according to the high resistance of the oxide layer, only part of the metal surface connects to the electrolyte through pathways in the coating. In the second model (Figure 10b) the first R-C element connected in series with the rest of the elements arranged as in the model (a). The connection of elements in series (Voight circuit) is typically applied for EIS fitting of sealed porous anodic oxide layers [78] and in some cases for sol-gel coated metals [44, 45]. In the case of EC model (Figure 10b) electrolyte has access to all oxide surface through even distribution of the pores in the sol-gel coating. At such condition the oxide film capacitance estimated from the sol-gel coated samples should be similar to the oxide film capacitance of uncoated aluminium samples. Figure 11 presents the EIS spectrum of sample Sg1Al10V and fitting lines according to the two EC described above. Both EC models overlap and give similar fitting quality, albeit slightly

different parameters (Table 4). The calculated oxide layer thicknesses (equations 2, 3) are 21 nm and 20 nm for EC models a) and b) respectively. In both cases the calculated oxide thickness is larger than the nominal oxide thickness (i.e. 14.2 nm) of the anodised sample Al10V. Although both models are applicable for EIS spectra fitting, the physical meaning of the model in Figure 10a better describes the properties of the sol-gel coated aluminium.

4.2. Interpretation of oxide layer properties via the analysis of EIS fitting results

There is a discrepancy concerning the interpretation of sol-gel coated aluminium EIS spectra. There are papers where the presence of barrier oxide layer was not considered and most often the time constant was assigned to corrosion process [51, 52]. However, the EIS fitting data presented in this work unambiguously proved that the middle frequency time constant observed on the sol-gel coated samples is related to the oxide film. It was demonstrated that upon increasing the barrier oxide film thickness on anodised aluminium samples the impedance grows proportionally to the oxide thickness (Figure 3). However, the oxide film thickness estimated from EIS spectra of the sol-gel coated samples is higher than that on bare anodised samples. A most probable cause for such an effect is the strong bonding between the sol-gel and oxide surface and, consequently, the blocking effect of the sol-gel coating against penetration of corrosive electrolyte to the oxide/sol-gel interface. This requires that the sol-gel coating covers some part of the oxide surface due to formation of chemical bonds between the hydroxyl groups located on the oxide surface and silanol groups and hydrolysed zirconium (IV) propoxide existing in the sol-gel formulation (Figure 10c). The electropolished aluminium had hydroxyl fraction about 0.57 (the peak area ratio of OH^- to O^{2-} components) upon exposure to the humidity level of 40 % for 240 min [79]. On the other hand, the anodised aluminium surfaces display a lower hydroxyl fraction of about 0.10-0.33 [80]. The studies of Alexander et al. revealed that the hydroxyl fraction of the electropolished aluminium and anodised aluminium was about 0.8 and 0.6 respectively [81]. In another work by the same group it was found that the hydroxyl fraction decreased with the increase of the anodised oxide film thickness in the range of 3-10 nm [82]. It is rational to say that the oxide surface having the lower OH fraction would have less efficient chemical bonding between the sol-gel and oxide surface. However, as was pointed out earlier, hybrid silanes cannot produce a uniform and consistent Si-O-Al bonds, and the sol-gel coated surface always contains patches with no chemical bonds due to steric hindrance of the silane molecules [76]. Therefore, the bonding strength between the sol-gel and oxide will depend on both hydroxyl fraction at the surface and sol-gel chemistry.

The adhesion quality at the sol-gel/oxide interface can be followed by EIS and in-depth analysis of the oxide film properties. More specifically the exposed surface area to the electrolyte (A_{exp}) is proportional to the oxide capacitance (C_{ox}) of the sol-gel coated sample divided by the oxide capacitance of uncoated sample (C^o_{ox}), or the oxide thickness of the uncoated substrate (d^o_{ox}) divided by the calculated oxide thickness of the coated one (d_{ox}) (equation 5):

$$A_{exp} = \frac{C_{ox}}{C^o_{ox}} \times 100\% = \frac{d^o_{ox}}{d_{ox}} \times 100\% \quad (5)$$

The difference between the calculated oxide thickness of the coated and uncoated aluminium is shown in Figure 12 a and Figure 12 b , using equations 1 and 2, respectively. Table 5 displays the exposed surface areas of the oxide for the different sol-gel coated samples, which were estimated using equation 5 and the values of C_{eff} (obtained using equations 1 and 2). As can be seen, the A_{exp} is consistent for the anodised samples studied in this work, though the two equations result in different estimates of the exposed surface area (Table 5). Considering that the electropolished surface had a higher hydroxyl fraction than the anodised surface [79-82] it can be assumed that the adhesion should be better and the exposed oxide area should be lower in this case (Table 5). Considering this evidence, it was established that equation 2 (assuming surface distribution of time constants) seems to be more appropriate for calculation of C_{eff} of the oxide film on the sol-gel coated aluminium (Table 5). It is suggested that the oxide film response in sol-gel coated samples is a sum of local $R_{ox}C_{ox}$ elements which distribute along the surface, as is shown in Figure 13a. Based on this discussion the degradation mechanism of the sol-gel coated aluminium samples most likely happens according to the scheme (Figure 13a,b). It involves the growth of the sol-gel porosity during immersion while the sol-gel/oxide interface remains unchanged. Normally local corrosion events on the metallic surface accelerate the degradation of the interface [56]. In this work a model aluminium/sol-gel system was designed to significantly decrease the degradation of the interface due to corrosion, which allowed to study the properties of the oxide layer by EIS.

4.3. Outlook on using EIS fitting for characterisation of sol-gel coated aluminium

By analysing the response of a coating using EIS one can understand the degradation kinetics of the coating and also demonstrate the self-healing properties of polymeric coatings [36, 54, 55]. The water uptake by the coating can be evaluated by monitoring the region on the Bode plots where the coating shows the capacitive response in the high-frequency range, i.e. a straight line with a slope close to -1 (Figure 14). Self-healing events in coatings are reflected in the behaviour of the coating resistance (R_{coat}). The value of the pore resistance of a coating is inversely proportional to the area of defects through the organic coating and is a measure of the coating degradation and indirectly of the electrochemically active surface area [56, 57]. Two factors contribute to the deadhesion of a coating, namely delamination and coating degradation. In section 4.2 it was demonstrated that the latter factor did not contribute to the delamination of the sol-gel coating from the oxide (Figure 9, 12). The oxide layer response in the EIS spectra is an important characteristic of aluminium and aluminium alloys [19, 33, 62]. It should be pointed out that a system comprised of an aluminium alloy coated by a sol-gel might have a different delamination mechanism because numerous alloy intermetallics develop cathodic activity during immersion leading to the increase of pH that deteriorates the stability of the sol-gel/oxide interface [5, 33]. This “deadhesion” event is schematically shown in Figure 14 as a decrease of impedance in the middle-frequency range where there is the capacitive contribution of the oxide film to the impedance.

In this work little attention was given to the corrosion process (Figure 5,14) because the used aluminium metal was relatively pure and was anodised, thus it did not show consistent

development of corrosion activity on the coated samples (Table 4). However, the corrosion activity quickly develops on the coated aluminium alloys during immersion tests [3, 83, 84]. The EIS was a common tool to assess self-healing properties of the coatings containing corrosion inhibitors without or with the presence of nanocontainers [85, 86]. In ref. [72] model corrosion studies were conducted on sol-gel coated AA2024 substrates. The EIS spectra recorded from the samples during immersion demonstrated that the time constant associated with corrosion (charge transfer resistance and double layer capacitance) was located in the low frequency range. Moreover, a testimony for that was the recovery of the impedance of the coated sample at the low frequency when a corrosion inhibitor was added to the corrosive electrolyte. When doubt exists whether a time constant is attributed to corrosion, dielectric oxide layer or mass transfer process it is a good practice to perform a control test employing corrosion inhibitors and prove the correct assignment of the time constant. The double layer capacitance (C_{dl}) parameter has been used for monitoring the delamination processes of the coated substrates [35, 36, 56]. The delaminated active area (A_d) is proportional to the ratio of C_{dl} to the specific double layer capacitance that can be measured on the bare metal (C^0_{dl}), assuming that the latter does not change during exposure to the electrolyte solution. However, in the context of this study such an assessment could not be done due to the local nature of corrosion that did not influence the properties of the oxide layer.

Conclusions

This work provided an insight into problems related with selection of equivalent circuit models for the fitting of EIS spectra of sol-gel coated aluminium samples and interpretation of the obtained fitting parameters. Model aluminium substrates were anodised producing different thicknesses of anodic aluminium oxide layers. Subsequently, the samples were coated and studied by EIS in a corrosive electrolyte.

EIS spectra of sol-gel coated substrates revealed the contribution of various interface phenomena to the impedance: the sol-gel film was in the higher frequency range, the oxide film was in the middle frequency range, while the corrosion process was visible at low frequency. The impedance response of the anodic oxide at middle frequency increased with the thickness of the oxide layers, which undoubtedly demonstrated the correctness of the applied equivalent circuit.

The effective capacitance (F/cm^2) of the barrier oxide in the sol-gel coated substrates was calculated using the capacitance–CPE relations from the work of Hirschorn et al. It was found that the equation (2) (formula of Brug et al.), assuming the surface distribution of the time constants, gave most adequate effective capacitance values.

An alternative assessment of the coating adhesion was proposed. The adhesion failure of the sol-gel coating was numerically calculated as the ratio of the effective oxide capacitance of the sol-gel coated samples to the effective oxide capacitance of the anodised samples.

During immersion in the electrolyte, the adhesive failure of the coating was relatively stable on all coated substrates, and by the end of immersion it was about 60-68 %. This

suggested that the degradation of the sol-gel coating growth of porosity during immersion did not contribute to the deadhesion of the coating.

Author Statement

K.A. Yasakau: Writing - Original Draft, Writing - Review & Editing, Conceptualization, Methodology, Validation, Investigation; **M. Starykevich**: Methodology, Validation, Investigation; **M.G.S. Ferreira**: Writing - Review & Editing; **M.L. Zheludkevich**: Conceptualization, Writing - Review & Editing, Funding acquisition.

Acknowledgments

KY thanks to the Portuguese Foundation for Science and Technology (FCT) and a researcher grant (IF/01284/2015). A part of this work was developed within the scope of the project CICECO-Aveiro Institute of Materials, UIDB/50011/2020 & UIDP/50011/2020, financed by national funds through the Portuguese Foundation for Science and Technology/MCTES.

References

[1] E.A. Starke, J.T. Staley, Application of modern aluminum alloys to aircraft, Progress in Aerospace Sciences, 32 (1996) 131-172. https://doi.org/10.1016/0376-0421(95)00004-6
[2] A.E. Hughes, A. Boag, A.M. Glenn, D. McCulloch, T.H. Muster, C. Ryan, C. Luo, X. Zhou, G.E. Thompson, Corrosion of AA2024-T3 Part II: Co-operative corrosion, Corros. Sci., 53 (2011) 27-39. https://doi.org/10.1016/j.corsci.2010.09.030
[3] N. Birbilis, R.G. Buchheit, Electrochemical Characteristics of Intermetallic Phases in Aluminum Alloys: An Experimental Survey and Discussion, J. Electrochem. Soc., 152 (2005) B140-B151. 10.1149/1.1869984
[4] R.G. Buchheit, R.P. Grant, P.F. Hlava, B. Mckenzie, G.L. Zender, Local Dissolution Phenomena Associated with S Phase (Al2CuMg) Particles in Aluminum Alloy 2024-T3, J. Electrochem. Soc., 144 (1997) 2621-2628. 10.1149/1.1837874
[5] C. Senöz, M. Rohwerder, Scanning Kelvin probe force microscopy for the in situ observation of the direct interaction between active head and intermetallic particles in filiform corrosion on aluminium alloy, Electrochim. Acta, 56 (2011) 9588-9595. https://doi.org/10.1016/j.electacta.2011.02.052
[6] H.N. McMurray, A. Holder, G. Williams, G.M. Scamans, A.J. Coleman, The kinetics and mechanisms of filiform corrosion on aluminium alloy AA6111, Electrochim. Acta, 55 (2010) 7843-7852. https://doi.org/10.1016/j.electacta.2010.04.035
[7] C. Luo, X. Zhou, G.E. Thompson, A.E. Hughes, Observations of intergranular corrosion in AA2024-T351: The influence of grain stored energy, Corros. Sci., 61 (2012) 35-44. https://doi.org/10.1016/j.corsci.2012.04.005
[8] S. Kumari, S. Wenner, J.C. Walmsley, O. Lunder, K. Nisancioglu, Progress in Understanding Initiation of Intergranular Corrosion on AA6005 Aluminum Alloy with Low Copper Content, J. Electrochem. Soc., 166 (2019) C3114-C3123. 10.1149/2.0211911jes
[9] R.L. Twite, G.P. Bierwagen, Review of alternatives to chromate for corrosion protection of aluminum aerospace alloys, Prog. Org. Coat., 33 (1998) 91-100. https://doi.org/10.1016/S0300-9440(98)00015-0
[10] S.M. Cohen, Review: Replacements for Chromium Pretreatments on Aluminum, Corrosion, 51 (1995) 71-78. 10.5006/1.3293580
[11] K.A. Yasakau, M.L. Zheludkevich, S.V. Lamaka, M.G.S. Ferreira, Mechanism of Corrosion Inhibition of AA2024 by Rare-Earth Compounds, J. Phys. Chem. B, 110 (2006) 5515-5528. 10.1021/jp0560664
[12] V.S. Sastri, Green Corrosion Inhibitors: Theory and Practice, Wiley2012.
[13] S.T. Abrahami, J.M.M. de Kok, H. Terryn, J.M.C. Mol, Towards Cr(VI)-free anodization of aluminum alloys for aerospace adhesive bonding applications: A review, Frontiers of Chemical Science and Engineering, 11 (2017) 465-482. 10.1007/s11705-017-1641-3
[14] G. Bierwagen, R. Brown, D. Battocchi, S. Hayes, Active metal-based corrosion protective coating systems for aircraft requiring no-chromate pretreatment, Prog. Org. Coat., 67 (2010) 195-208. https://doi.org/10.1016/j.porgcoat.2009.10.009
[15] G.W. Critchlow, D.M. Brewis, Review of surface pretreatments for aluminium alloys, Int. J. Adhes. Adhes., 16 (1996) 255-275. https://doi.org/10.1016/S0143-7496(96)00014-0
[16] G.W. Critchlow, K.A. Yendall, D. Bahrani, A. Quinn, F. Andrews, Strategies for the replacement of chromic acid anodising for the structural bonding of aluminium alloys, Int. J. Adhes. Adhes., 26 (2006) 419-453. https://doi.org/10.1016/j.ijadhadh.2005.07.001
[17] P. Campestrini, H. Terryn, A. Hovestad, J.H.W. de Wit, Formation of a cerium-based conversion coating on AA2024: relationship with the microstructure, Surf. Coat. Technol., 176 (2004) 365-381. https://doi.org/10.1016/S0257-8972(03)00743-6

[18] M.L. Zheludkevich, I.M. Salvado, M.G.S. Ferreira, Sol–gel coatings for corrosion protection of metals, J. Mater. Chem., 15 (2005) 5099-5111. 10.1039/B419153F
[19] K.A. Yasakau, A. Kuznetsova, S. Kallip, M. Starykevich, J. Tedim, M.G.S. Ferreira, M.L. Zheludkevich, A novel bilayer system comprising LDH conversion layer and sol-gel coating for active corrosion protection of AA2024, Corros. Sci., 143 (2018) 299-313. https://doi.org/10.1016/j.corsci.2018.08.039
[20] A.F. Carreira, A.M. Pereira, E.P. Vaz, A.M. Cabral, T. Ghidini, L. Pigliaru, T. Rohr, Alternative corrosion protection pretreatments for aluminum alloys, Journal of Coatings Technology and Research, 14 (2017) 879-892. 10.1007/s11998-017-9922-9
[21] A. De Nicolò, L. Paussa, A. Gobessi, A. Lanzutti, C. Cepek, F. Andreatta, L. Fedrizzi, Cerium conversion coating and sol–gel multilayer system for corrosion protection of AA6060, Surf. Coat. Technol., 287 (2016) 33-43. https://doi.org/10.1016/j.surfcoat.2015.12.059
[22] M. Poberžnik, D. Costa, A. Hemeryck, A. Kokalj, Insight into the Bonding of Silanols to Oxidized Aluminum Surfaces, The Journal of Physical Chemistry C, 122 (2018) 9417-9431. 10.1021/acs.jpcc.7b12552
[23] D. Balgude, A. Sabnis, Sol–gel derived hybrid coatings as an environment friendly surface treatment for corrosion protection of metals and their alloys, J. Sol-Gel Sci. Technol., 64 (2012) 124-134. 10.1007/s10971-012-2838-z
[24] K.A. Yasakau, J. Tedim, M.L. Zheludkevich, R. Drumm, M. Shem, M. Wittmar, M. Veith, M.G.S. Ferreira, Cerium molybdate nanowires for active corrosion protection of aluminium alloys, Corros. Sci., 58 (2012) 41-51. https://doi.org/10.1016/j.corsci.2012.01.012
[25] K.A. Yasakau, J. Tedim, M.L. Zheludkevich, M.G.S. Ferreira, Active Corrosion Protection by Nanoparticles and Conversion Films of Layered Double Hydroxides, CORROSION, 70 (2014) 436-445. 10.5006/0979
[26] K.A. Yasakau, M.L. Zheludkevich, O.V. Karavai, M.G.S. Ferreira, Influence of inhibitor addition on the corrosion protection performance of sol–gel coatings on AA2024, Prog. Org. Coat., 63 (2008) 352-361. https://doi.org/10.1016/j.porgcoat.2007.12.002
[27] Y. Zhang, P. Yu, J. Wu, F. Chen, Y. Li, Y. Zhang, Y. Zuo, Y. Qi, Enhancement of anticorrosion protection via inhibitor-loaded ZnAlCe-LDH nanocontainers embedded in sol–gel coatings, Journal of Coatings Technology and Research, 15 (2018) 303-313. 10.1007/s11998-017-9978-6
[28] N. LeBozec, N. Blandin, D. Thierry, Accelerated corrosion tests in the automotive industry: A comparison of the performance towards cosmetic corrosion, Mater. Corros., 59 (2008) 889-894. https://doi.org/10.1002/maco.200804168
[29] C.L. Meade, Accelerated corrosion testing, Metal Finishing, 98 (2000) 540-545. https://doi.org/10.1016/S0026-0576(00)80461-4
[30] R.G. Kelly, J.R. Scully, D. Shoesmith, R.G. Buchheit, Electrochemical Techniques in Corrosion Science and Engineering, CRC Press2002.
[31] P.L. Bonora, F. Deflorian, L. Fedrizzi, Electrochemical impedance spectroscopy as a tool for investigating underpaint corrosion, Electrochim. Acta, 41 (1996) 1073-1082. https://doi.org/10.1016/0013-4686(95)00440-8
[32] G. Grundmeier, W. Schmidt, M. Stratmann, Corrosion protection by organic coatings: electrochemical mechanism and novel methods of investigation, Electrochim. Acta, 45 (2000) 2515-2533. https://doi.org/10.1016/S0013-4686(00)00348-0
[33] K.A. Yasakau, J. Carneiro, M.L. Zheludkevich, M.G.S. Ferreira, Influence of sol-gel process parameters on the protection properties of sol–gel coatings applied on AA2024, Surf. Coat. Technol., 246 (2014) 6-16. https://doi.org/10.1016/j.surfcoat.2014.02.038
[34] G.W. Walter, A review of impedance plot methods used for corrosion performance analysis of painted metals, Corros. Sci., 26 (1986) 681-703. https://doi.org/10.1016/0010-938X(86)90033-8

[35] A. Amirudin, D. Thieny, Application of electrochemical impedance spectroscopy to study the degradation of polymer-coated metals, Prog. Org. Coat., 26 (1995) 1-28. https://doi.org/10.1016/0300-9440(95)00581-1
[36] M. Abdolah Zadeh, S. van der Zwaag, S.J. García, Assessment of healed scratches in intrinsic healing coatings by AC/DC/AC accelerated electrochemical procedure, Surf. Coat. Technol., 303 (2016) 396-405. https://doi.org/10.1016/j.surfcoat.2015.11.001
[37] S.J. García, J. Suay, Optimization of deposition voltage of cataphoretic automotive primers assessed by EIS and AC/DC/AC, Prog. Org. Coat., 66 (2009) 306-313. https://doi.org/10.1016/j.porgcoat.2009.08.012
[38] F. Mahdavi, M.Y.J. Tan, M. Forsyth, Electrochemical impedance spectroscopy as a tool to measure cathodic disbondment on coated steel surfaces: Capabilities and limitations, Prog. Org. Coat., 88 (2015) 23-31. https://doi.org/10.1016/j.porgcoat.2015.06.010
[39] B.R. Hinderliter, S.G. Croll, D.E. Tallman, Q. Su, G.P. Bierwagen, Interpretation of EIS data from accelerated exposure of coated metals based on modeling of coating physical properties, Electrochim. Acta, 51 (2006) 4505-4515. https://doi.org/10.1016/j.electacta.2005.12.047
[40] Y.-M. Chen, A.S. Nguyen, M.E. Orazem, B. Tribollet, N. Pébère, M. Musiani, V. Vivier, Identification of Resistivity Distributions in Dielectric Layers by Measurement Model Analysis of Impedance Spectroscopy, Electrochim. Acta, 219 (2016) 312-320. https://doi.org/10.1016/j.electacta.2016.09.136
[41] A.S. Nguyen, M. Musiani, M.E. Orazem, N. Pébère, B. Tribollet, V. Vivier, Impedance analysis of the distributed resistivity of coatings in dry and wet conditions, Electrochim. Acta, 179 (2015) 452-459. https://doi.org/10.1016/j.electacta.2015.02.109
[42] G. Bouvet, D.D. Nguyen, S. Mallarino, S. Touzain, Analysis of the non-ideal capacitive behaviour for high impedance organic coatings, Prog. Org. Coat., 77 (2014) 2045-2053. https://doi.org/10.1016/j.porgcoat.2014.02.008
[43] E. Cavalcanti, O. Ferraz, A.R. Di Sarli, The use of electrochemical impedance measurements to assess the performance of organic coating systems on naval steel, Prog. Org. Coat., 23 (1993) 185-200. https://doi.org/10.1016/0033-0655(93)80010-8
[44] X. Yuan, Z.F. Yue, X. Chen, S.F. Wen, L. Li, T. Feng, The protective and adhesion properties of silicone-epoxy hybrid coatings on 2024 Al-alloy with a silane film as pretreatment, Corros. Sci., 104 (2016) 84-97. https://doi.org/10.1016/j.corsci.2015.11.035
[45] E. Bakhshandeh, A. Jannesari, Z. Ranjbar, S. Sobhani, M.R. Saeb, Anti-corrosion hybrid coatings based on epoxy–silica nano-composites: Toward relationship between the morphology and EIS data, Prog. Org. Coat., 77 (2014) 1169-1183. https://doi.org/10.1016/j.porgcoat.2014.04.005
[46] M.L. Zheludkevich, R. Serra, M.F. Montemor, K.A. Yasakau, I.M.M. Salvado, M.G.S. Ferreira, Nanostructured sol–gel coatings doped with cerium nitrate as pre-treatments for AA2024-T3: Corrosion protection performance, Electrochim. Acta, 51 (2005) 208-217. https://doi.org/10.1016/j.electacta.2005.04.021
[47] M. Schem, T. Schmidt, J. Gerwann, M. Wittmar, M. Veith, G.E. Thompson, I.S. Molchan, T. Hashimoto, P. Skeldon, A.R. Phani, S. Santucci, M.L. Zheludkevich, CeO2-filled sol–gel coatings for corrosion protection of AA2024-T3 aluminium alloy, Corros. Sci., 51 (2009) 2304-2315. https://doi.org/10.1016/j.corsci.2009.06.007
[48] S. Tajima, Anodic Oxidation of Aluminum, in: M.G. Fontana, R.W. Staehle (Eds.) Advances in Corrosion Science and Technology: Volume 1, Springer US, Boston, MA, 1970, pp. 229-362.
[49] C. Vargel, Chapter B.1 - Introducton to The Corrosion of Aluminium, in: C. Vargel (Ed.) Corrosion of Aluminium, Elsevier, Amsterdam, 2004, pp. 81-109.

[50] G.E. Thompson, Porous anodic alumina: fabrication, characterization and applications, Thin Solid Films, 297 (1997) 192-201. https://doi.org/10.1016/S0040-6090(96)09440-0
[51] M.-Y. Jiang, L.-K. Wu, J.-M. Hu, J.-Q. Zhang, Silane-incorporated epoxy coatings on aluminum alloy (AA2024). Part 1: Improved corrosion performance, Corros. Sci., 92 (2015) 118-126. https://doi.org/10.1016/j.corsci.2014.11.046
[52] T.L. Metroke, J.S. Gandhi, A. Apblett, Corrosion resistance properties of Ormosil coatings on 2024-T3 aluminum alloy, Prog. Org. Coat., 50 (2004) 231-246. https://doi.org/10.1016/j.porgcoat.2004.03.001
[53] D. Zhu, W.J. van Ooij, Corrosion protection of AA 2024-T3 by bis-[3-(triethoxysilyl)propyl]tetrasulfide in sodium chloride solution.: Part 2: mechanism for corrosion protection, Corros. Sci., 45 (2003) 2177-2197. https://doi.org/10.1016/S0010-938X(03)00061-1
[54] A. Lutz, O. van den Berg, J. Wielant, I. De Graeve, H. Terryn, A Multiple-Action Self-Healing Coating, Frontiers in Materials, 2 (2016). 10.3389/fmats.2015.00073
[55] S. van der Zwaag, E. Brinkman, Self Healing Materials: Pioneering Research in the Netherlands, IOS Press2015.
[56] F. Deflorian, L. Fedrizzi, Adhesion characterization of protective organic coatings by electrochemical impedance spectroscopy, J. Adhes. Sci. Technol., 13 (1999) 629-645. 10.1163/156856199X00154
[57] R. Hirayama, S. Haruyama, Electrochemical Impedance for Degraded Coated Steel Having Pores, Corrosion, 47 (1991) 952-958. 10.5006/1.3585208
[58] Z. Feng, G.S. Frankel, Evaluation of Coated Al Alloy Using the Breakpoint Frequency Method, Electrochim. Acta, 187 (2016) 605-615. https://doi.org/10.1016/j.electacta.2015.11.114
[59] C.H. Hsu, F. Mansfeld, Technical Note: Concerning the Conversion of the Constant Phase Element Parameter Y0 into a Capacitance, CORROSION, 57 (2001) 747-748. 10.5006/1.3280607
[60] G.J. Brug, A.L.G. van den Eeden, M. Sluyters-Rehbach, J.H. Sluyters, The analysis of electrode impedances complicated by the presence of a constant phase element, Journal of Electroanalytical Chemistry and Interfacial Electrochemistry, 176 (1984) 275-295. https://doi.org/10.1016/S0022-0728(84)80324-1
[61] B. Hirschorn, M.E. Orazem, B. Tribollet, V. Vivier, I. Frateur, M. Musiani, Determination of effective capacitance and film thickness from constant-phase-element parameters, Electrochim. Acta, 55 (2010) 6218-6227. http://dx.doi.org/10.1016/j.electacta.2009.10.065
[62] K.A. Yasakau, A.N. Salak, M.L. Zheludkevich, M.G.S. Ferreira, Volta Potential of Oxidized Aluminum Studied by Scanning Kelvin Probe Force Microscopy, The Journal of Physical Chemistry C, 114 (2010) 8474-8484. 10.1021/jp1011044
[63] J. Hitzig, K. Jüttner, W.J. Lorenz, W. Paatsch, AC-impedance measurements on porous aluminium oxide films, Corros. Sci., 24 (1984) 945-952. https://doi.org/10.1016/0010-938X(84)90115-X
[64] T.W. Hickmott, Interface states at the anodized Al2O3-metal interface, J. Appl. Phys., 89 (2001) 5502-5508. 10.1063/1.1366653
[65] M.M. Lohrengel, Thin anodic oxide layers on aluminium and other valve metals: high field regime, Materials Science and Engineering: R: Reports, 11 (1993) 243-294. https://doi.org/10.1016/0927-796X(93)90005-N
[66] J.C. Barbour, R.G. Copeland, R.G. Dunn, N. Missert, L.P. Montes, K.-A. Son, J.P. Sullivan, The Electrical Properties of Native and Deposited Thin Aluminum Oxide Layers on Aluminum: Hydration Effects, Electrochemical Society Pennington, New Jersey 1998.
[67] J.-K. Chang, C.-M. Liao, C.-H. Chen, W.-T. Tsai, Microstructure and Electrochemical Characteristics of Aluminum Anodized Film Formed in Ammonium Adipate Solution, J. Electrochem. Soc., 150 (2003) B266. 10.1149/1.1570822

[68] J.W. Diggle, T.C. Downie, C.W. Goulding, Anodic oxide films on aluminum, Chem. Rev., 69 (1969) 365-405. 10.1021/cr60259a005
[69] M.J. Dignam, Oxide Films on Aluminum, Journal of The Electrochemical Society, 109 (1962) 192. 10.1149/1.2425369
[70] M.J. Dignam, Oxide Films on Aluminum, J. Electrochem. Soc., 109 (1962) 184. 10.1149/1.2425368
[71] P. Álvarez, A. Collazo, A. Covelo, X.R. Nóvoa, C. Pérez, The electrochemical behaviour of sol–gel hybrid coatings applied on AA2024-T3 alloy: Effect of the metallic surface treatment, Prog. Org. Coat., 69 (2010) 175-183. https://doi.org/10.1016/j.porgcoat.2010.04.005
[72] M.L. Zheludkevich, K.A. Yasakau, A.C. Bastos, O.V. Karavai, M.G.S. Ferreira, On the application of electrochemical impedance spectroscopy to study the self-healing properties of protective coatings, Electrochem. Commun., 9 (2007) 2622-2628. https://doi.org/10.1016/j.elecom.2007.08.012
[73] H.-C. You, C.-M. Chang, T.-F. Liu, C.-C. Cheng, F.-C. Chang, F.-H. Ko, Facile preparation of sol–gel-derived ultrathin and high-dielectric zirconia films for capacitor devices, Appl. Surf. Sci., 258 (2012) 10084-10088. https://doi.org/10.1016/j.apsusc.2012.06.079
[74] D.M. Brasher, A.H. Kingsbury, Electrical measurements in the study of immersed paint coatings on metal. I. Comparison between capacitance and gravimetric methods of estimating water-uptake, Journal of Applied Chemistry, 4 (1954) 62-72. https://doi.org/10.1002/jctb.5010040202
[75] M. Pourbaix, Atlas of Electrochemical Equilibria in Aqueous Solutions, National Association of Corrosion Engineers1974.
[76] M. Poberžnik, A. Kokalj, Implausibility of bidentate bonding of the silanol headgroup to oxidized aluminum surfaces, Appl. Surf. Sci., 492 (2019) 909-918. https://doi.org/10.1016/j.apsusc.2019.04.032
[77] J.-B. Cambon, J. Esteban, F. Ansart, J.-P. Bonino, V. Turq, S.H. Santagneli, C.V. Santilli, S.H. Pulcinelli, Effect of cerium on structure modifications of a hybrid sol–gel coating, its mechanical properties and anti-corrosion behavior, Mater. Res. Bull., 47 (2012) 3170-3176. https://doi.org/10.1016/j.materresbull.2012.08.034
[78] J.A. González, V. López, A. Bautista, E. Otero, X.R. Nóvoa, Characterization of porous aluminium oxide films from a.c. impedance measurements, J. Appl. Electrochem., 29 (1999) 229-238. 10.1023/A:1003481418291
[79] Ö. Özkanat, B. Salgin, M. Rohwerder, J.M.C. Mol, J.H.W. de Wit, H. Terryn, Scanning Kelvin Probe Study of (Oxyhydr)oxide Surface of Aluminum Alloy, The Journal of Physical Chemistry C, 116 (2012) 1805-1811. 10.1021/jp205585u
[80] S.T. Abrahami, T. Hauffman, J.M.M. de Kok, J.M.C. Mol, H. Terryn, Effect of Anodic Aluminum Oxide Chemistry on Adhesive Bonding of Epoxy, The Journal of Physical Chemistry C, 120 (2016) 19670-19677. 10.1021/acs.jpcc.6b04957
[81] M.R. Alexander, G. Beamson, P. Bailey, T.C.Q. Noakes, P. Skeldon, G.E. Thompson, The distribution of hydroxyl ions at the surface of anodic alumina, Surf. Interface Anal., 35 (2003) 649-657. https://doi.org/10.1002/sia.1585
[82] M.R. Alexander, G.E. Thompson, X. Zhou, G. Beamson, N. Fairley, Quantification of oxide film thickness at the surface of aluminium using XPS, Surf. Interface Anal., 34 (2002) 485-489. https://doi.org/10.1002/sia.1344
[83] J. Li, N. Birbilis, R.G. Buchheit, Electrochemical assessment of interfacial characteristics of intermetallic phases present in aluminium alloy 2024-T3, Corros. Sci., 101 (2015) 155-164. https://doi.org/10.1016/j.corsci.2015.09.012
[84] S.V. Lamaka, M.L. Zheludkevich, K.A. Yasakau, M.F. Montemor, M.G.S. Ferreira, High effective organic corrosion inhibitors for 2024 aluminium alloy, Electrochim. Acta, 52 (2007) 7231-7247. https://doi.org/10.1016/j.electacta.2007.05.058

[85] U. Tiringer, A. Durán, Y. Castro, I. Milošev, Self-Healing Effect of Hybrid Sol-Gel Coatings Based on GPTMS, TEOS, SiO2Nanoparticles and Ce(NO3)3Applied on Aluminum Alloy 7075-T6, J. Electrochem. Soc., 165 (2018) C213-C225. 10.1149/2.0211805jes
[86] T. Wang, J. Du, S. Ye, L. Tan, J. Fu, Triple-Stimuli-Responsive Smart Nanocontainers Enhanced Self-Healing Anticorrosion Coatings for Protection of Aluminum Alloy, ACS Applied Materials & Interfaces, 11 (2019) 4425-4438. 10.1021/acsami.8b19950

Figure captions

Figure 1. AFM topography of aluminium samples before anodising (0V), and after anodising at 10V, 20V and 40V.

Figure 2. GDOES profiles across the control high purity aluminium samples anodised at 20 V and 40 V.

Figure 3. Bode plots of Al samples before anodising (A0V) and after anodising at 10 V, 20 V and 40 V (A10V, A20V and A40V respectively); the equivalent circuit selected for fitting is presented as an inset in Figure a).

Figure 4. SEM cross-section image (a) of epoxy resin (I) sol-gel coating (II) and aluminium (III), and GDOES profiles (b) obtained from the sol-gel coated samples.

Figure 5. Bode plots of Sg1Al0V, Sg1Al10V, Sg1Al20V and Sg1Al40V after 1 and 23 days of immersion in 0.5 M NaCl.

Figure 6. Equivalent circuit models used for fitting EIS spectra of the coated aluminium samples.

Figure 7. The evolution of $C_{coat\ eff}$ (a,c), water uptake (b) and R_{coat} (d) during immersion in 0.5 M NaCl; the $C_{coat\ eff}$ values were obtained from two equations 1 and 2.

Figure 8. Evolution of the oxide layer resistance (R_{ox}) during immersion in 0.5 M NaCl.

Figure 9. Aluminium oxide layer thickness calculated for samples Sg1Al0V (a), Sg1Al10V (b), Sg1Al20V (c) and Sg1Al40V (d) during immersion in 0.5 M NaCl; EIS fitting was done using EC model (Figure 6b).

Figure 10. A scheme of two EC models with the arrangement of elements in the hierarchical model (a) and in the series combination model (b); the interface between the sol-gel and oxide (c).

Figure 11. EIS spectrum of sample Sg1Al10V after 1 day of immersion and fit lines using EC models shown in Figure 10.

Figure 12. The calculated thickness of the aluminium oxide layer of sol-gel coated and uncoated samples; oxide thickness was obtained using equation 1 (a) and equation 2 (b).

Figure 13. Degradation mechanism of the sol-gel coated anodised aluminium samples during immersion.

Figure 14. A schematic representation of Bode plots demonstrating the degradation/healing events in the coating, deadhesion at the oxide/coating interface and corrosion and inhibition phenomena.

Table 1. Oxide film thickness grown on pure aluminium determined by GDOES.

Sample name	Anodising voltage	Average thickness, nm
Al0V		
Al10V	10V	14.2±0.8
Al20V	20V	26.9±1.1
Al40V	40V	53.7±0.9

Table 2. The capacitance of the oxide films calculated from EIS spectra and the relative dielectric constants calculated from equation 3.

Sample name	average C, F/cm^2	relative dielectric constant
Al0V	3.92E-06	9*
Al10V	5.73E-07	9.2±0.6
Al20V	3.15E-07	9.6±0.5
Al40V	1.65E-07	10.0±0.6

*Assumed value

Table 3. Fitted parameter values using the EC model presented in Figure 6b.

Parameters	Sg1Al0V		Sg1Al10V		Sg1Al20V		Sg1Al40V	
	1day	23days	1day	23days	1day	23days	1day	23days
CPE_{coat} ($nS\ s^{-a}\ cm^{-2}$)	42.9±4	145±31	46.1±6	71.7±2	46.3±6	69.3±16	33.0±4.5	47.8±9
a_coat	0.833±0.01	0.773±0.02	0.837±0.01	0.841±0.02	0.836±0.01	0.844±0.02	0.861±0.01	0.872±0.02
R_{coat} ($k\Omega\ cm^2$)	7.94±0.1	1.26±0.03	5.43±0.1	0.901±0.03	5.77±0.13	0.956±0.03	6.30±0.02	0.984±0.04
CPE_{ox} ($\mu S\ s^{-a}\ cm^{-2}$)	2.79±0.04	2.82±0.05	0.415±0.01	0.409±0.18	0.215±0.06	0.211±0.01	0.112±0.04	0.109±0.08
$a_{\_ox}$	0.955±0.01	0.966±0.01	0.989±0.01	0.995±0.01	0.997±0.05	1±0.01	1±0.01	1±0.01
R_{ox} ($M\Omega\ cm^2$)	8.97±2.5	2.04±0.1	30.8±3.7	17.7±17	143±20	32.5±4	281±62	360±203
CPE_{dl} ($\mu S\ s^{-a}\ cm^{-2}$)	4.22±4.2	16.5±5	0.597±0.28	0.039±0.016	0.225±0.05	0.635±0.3	0.223±0.22	0.067±0.07
$a_{\_dl}$	1±0.9	1±0.08	0.933±0.1	0.870±0.1	1±0.3	0.923±0.1	1±0.5	0.970±0.4
R_{ct} ($M\Omega\ cm^2$)	19.1±19	2.82±0.4	59.1±12.9	684±216	161±23	41.2±9	171±160	418±310
Chi^2 (10^{-4})	3.41	2.84	2.15	1.20	2.55	2.29	3.80	2.30

Table 4. Fitted parameter values of EIS spectrum shown in Figure 10 using the EC models presented in Figure 9.

Parameters/Systems	Sg1Al10V	
	Model a	Model b
CPE_{coat} ($nS\ s^{-a}\ cm^{-2}$)	46.1±6	41.6±5
a_coat	0.837±0.01	0.847±0.01
R_{coat} ($k\Omega\ cm^2$)	5.43±0.1	5.02±0.08
CPE_{ox} ($\mu S\ s^{-a}\ cm^{-2}$)	0.415±0.01	0.457±0.01
$a_{\_ox}$	0.989±0.01	0.981±0.04
R_{ox} ($M\Omega\ cm^2$)	30.8±3.7	27.0±3.7
CPE_{dl} ($\mu S\ s^{-a}\ cm^{-2}$)	0.597±0.28	0.479±0.22
$a_{\_dl}$	0.933±0.1	0.880±0.1
R_{ct} ($M\Omega\ cm^2$)	59.1±12.9	65.7±14.7
Chi^2 (10^{-4})	2.15	1.87

Table 5. The exposed surface area (A_{exp}), which was calculated using equation 5 and different effective capacitance values (equations 1 and 2), of the oxide in the sol-gel coated samples after immersion.

Sample name	Surface area, % Equation (1)	Surface area, % Equation (2)
Sg1Al0V	80.7	60.4
Sg1Al10V	73.6	68.5
Sg1Al20V	68.8	66.6
Sg1Al40V	69.3	66.0

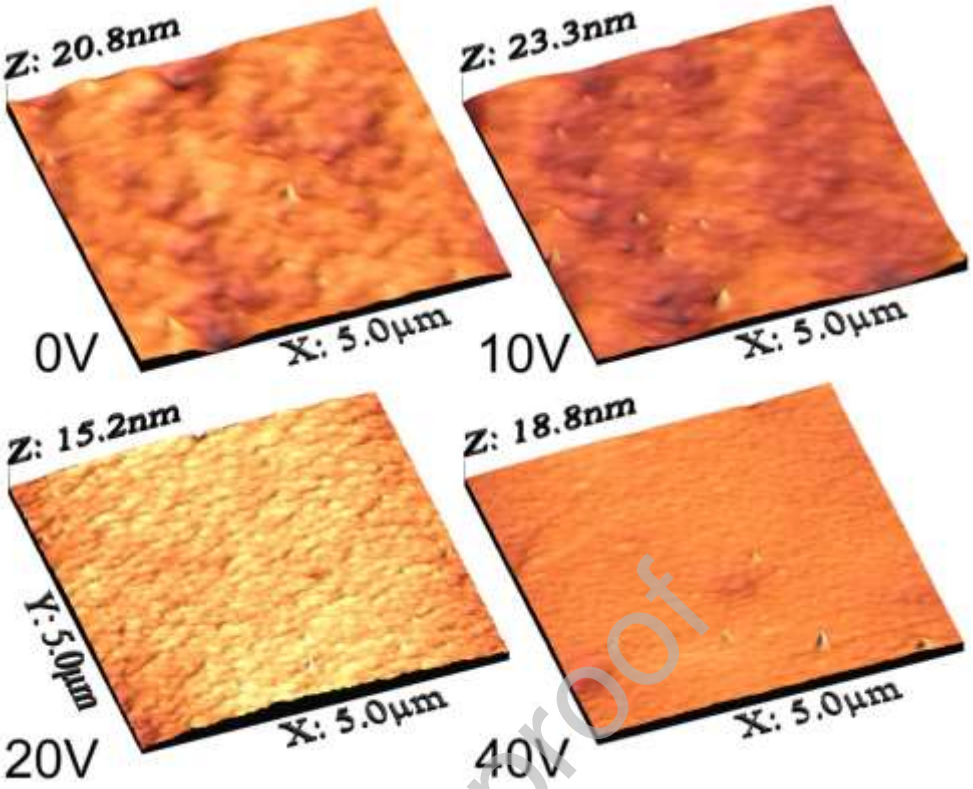

Figure 1. AFM topography of aluminium samples before anodising (0V), and after anodising at 10V, 20V and 40V.

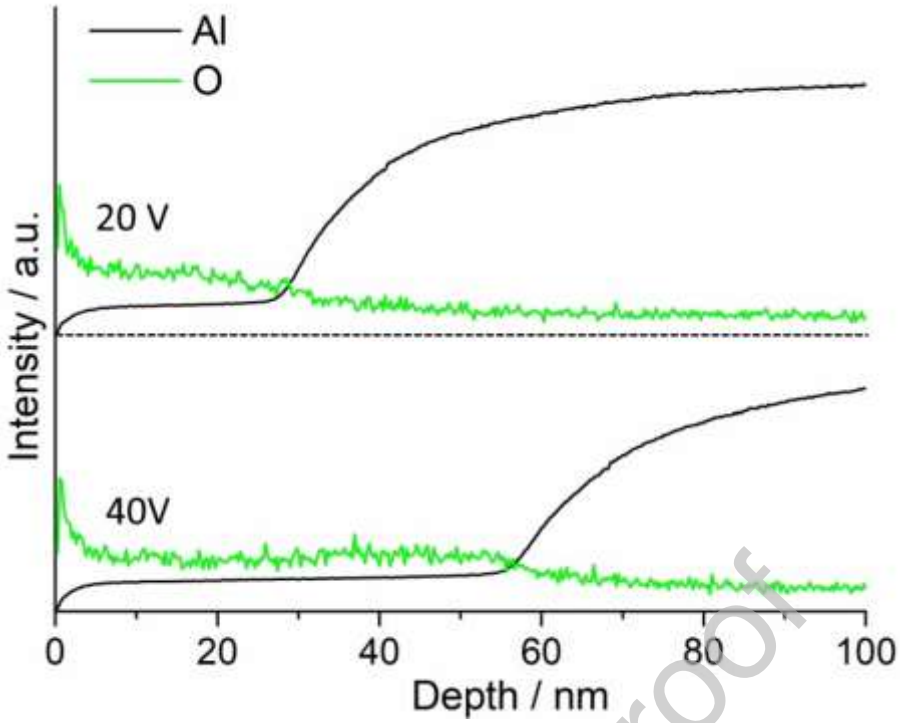

Figure 2. GDOES profiles across the control high purity aluminium samples anodised at 20 V and 40 V.

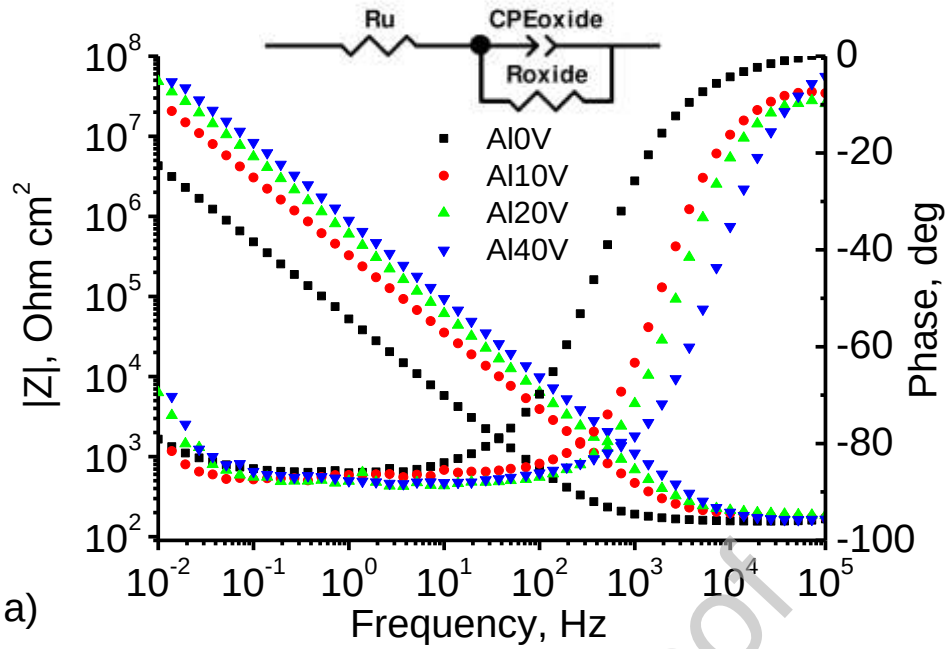

Figure 3. Bode plots of Al samples before anodising (A0V) and after anodising at 10 V, 20 V and 40 V (A10V, A20V and A40V respectively); the equivalent circuit selected for fitting is presented as an inset in Figure a).

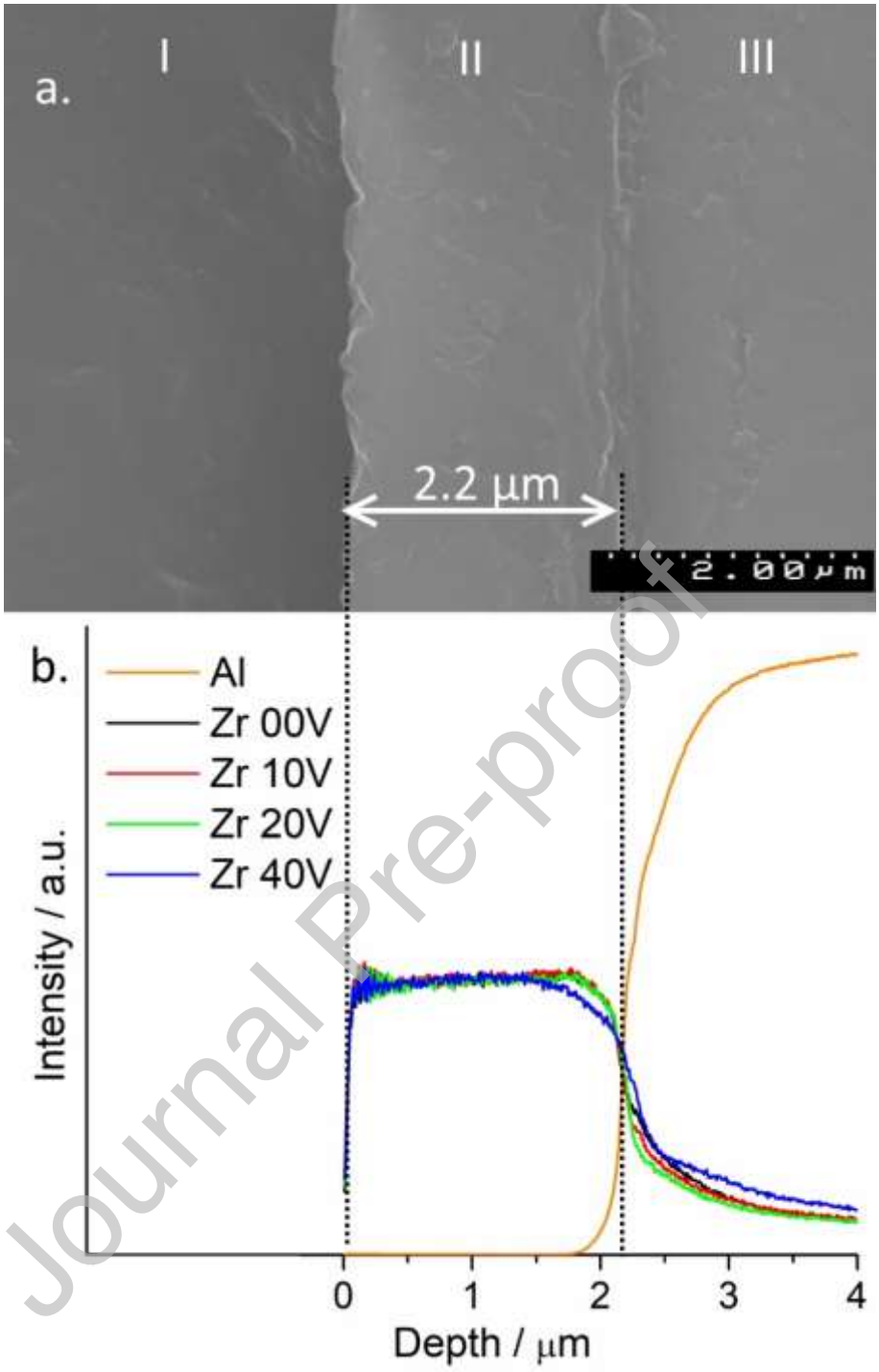

Figure 4. SEM cross-section image (a) of epoxy resin (I) sol-gel coating (II) and aluminium (III), and GDOES profiles (b) obtained from the sol-gel coated samples.

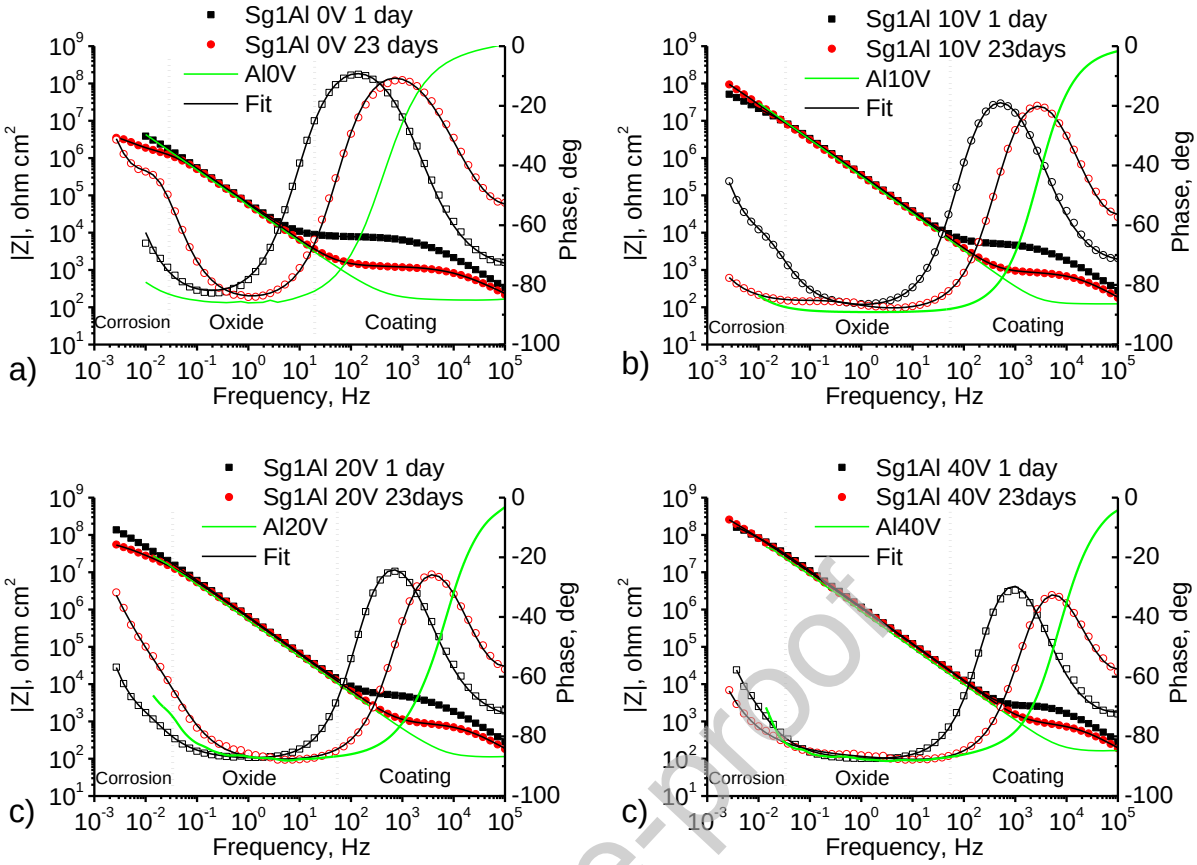

Figure 5. Bode plots of Sg1Al0V, Sg1Al10V, Sg1Al20V and Sg1Al40V after 1 and 23 days of immersion in 0.5 M NaCl.

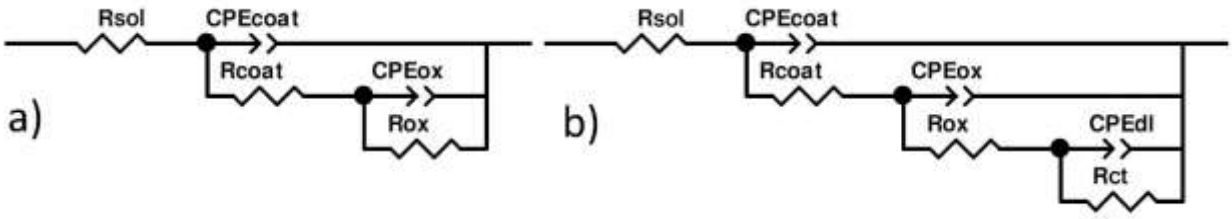

Figure 6. Equivalent circuit models used for fitting EIS spectra of the coated aluminium samples.

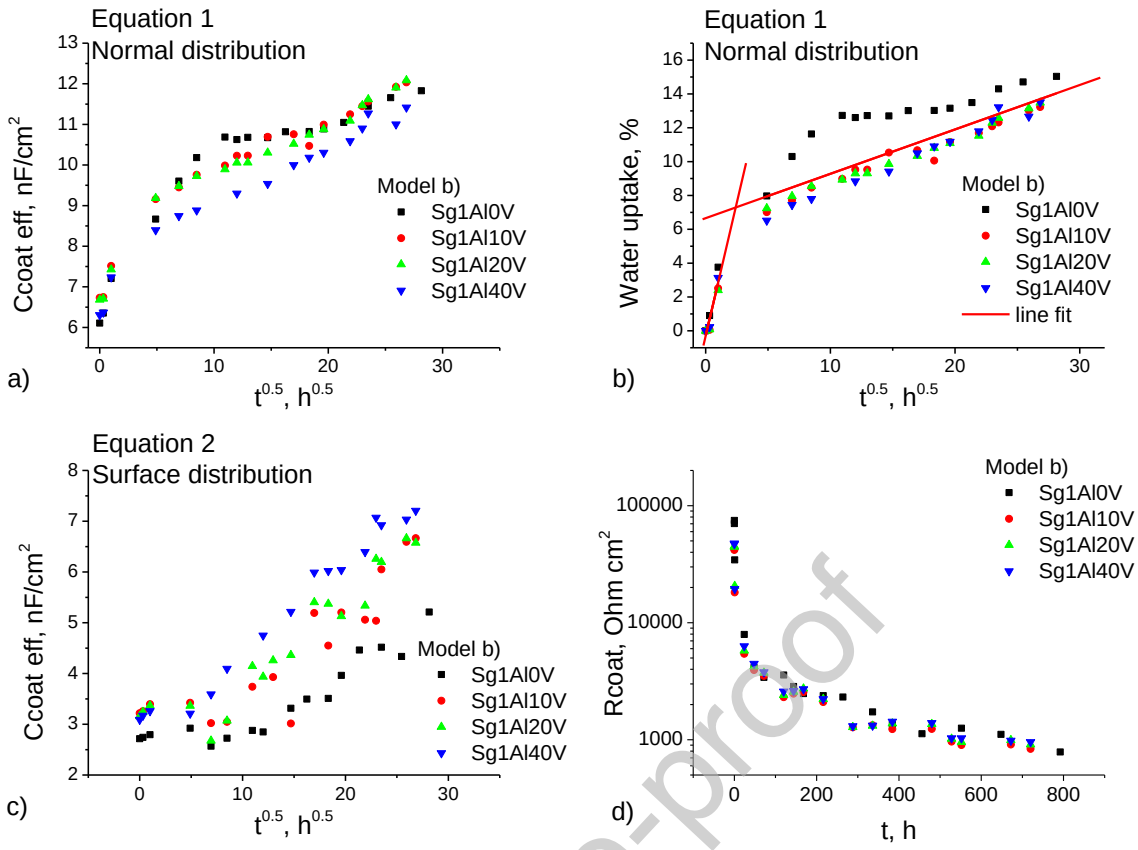

Figure 7. The evolution of $C_{coat\ eff}$ (a,c), water uptake (b) and R_{coat} (d) during immersion in 0.5 M NaCl; the $C_{coat\ eff}$ values were obtained from two equations 1 and 2.

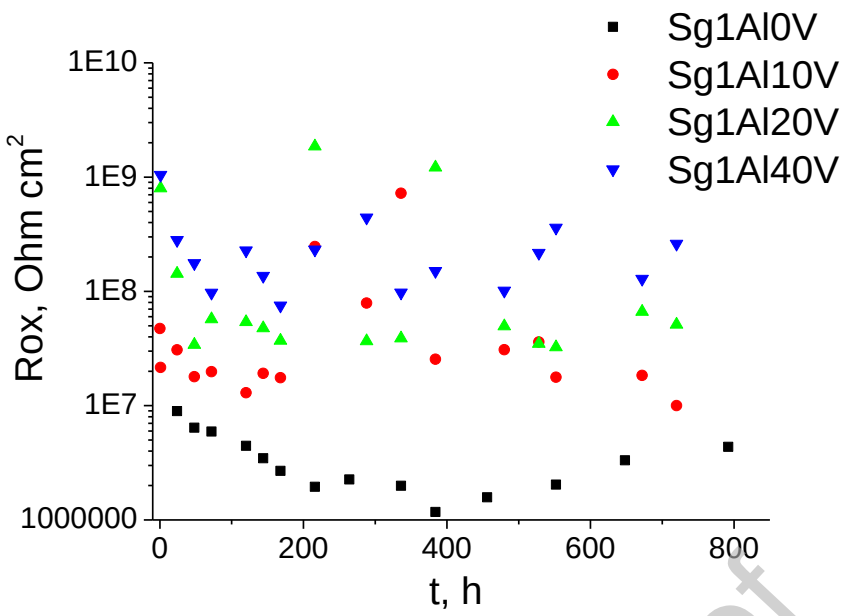

Figure 8. Evolution of the oxide layer resistance (R_{ox}) during immersion in 0.5 M NaCl.

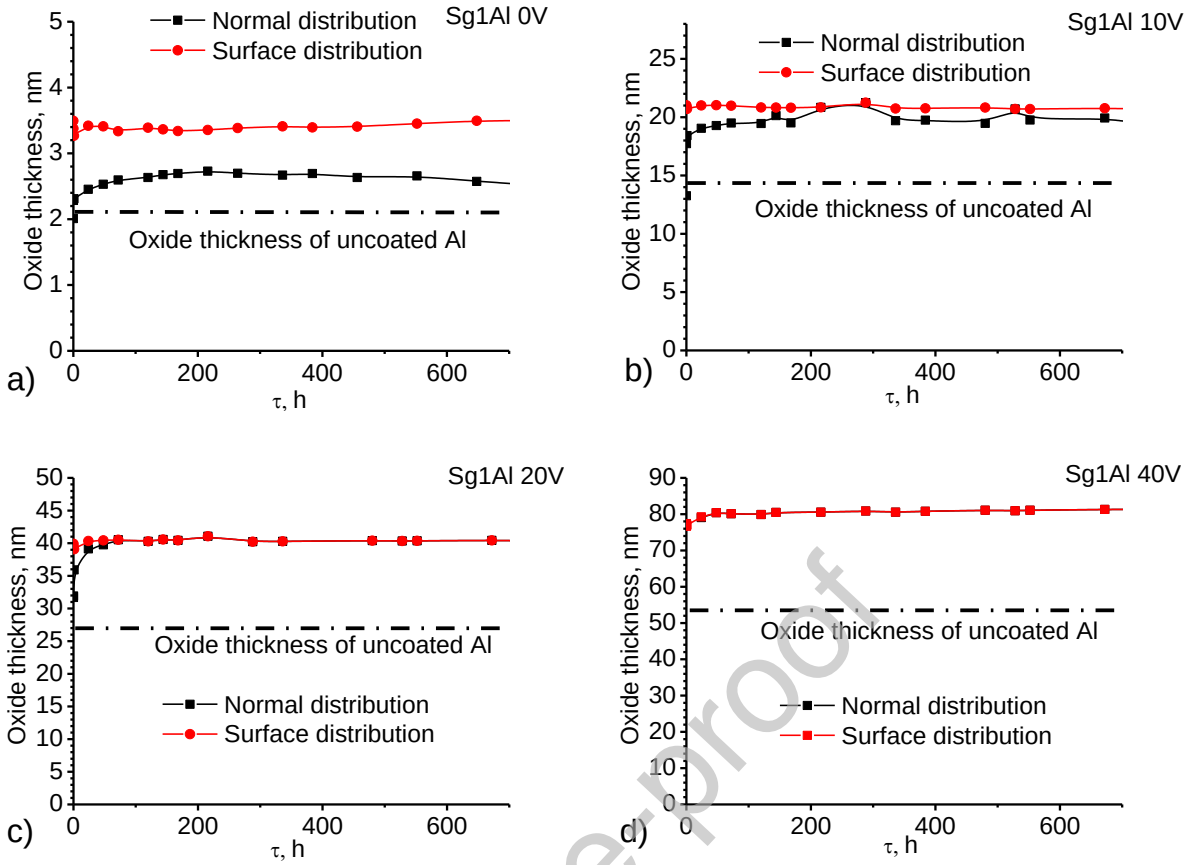

Figure 9. Aluminium oxide layer thickness calculated for samples Sg1Al0V (a), Sg1Al10V (b), Sg1Al20V (c) and Sg1Al40V (d) during immersion in 0.5 M NaCl; EIS fitting was done using EC model (Figure 6b).

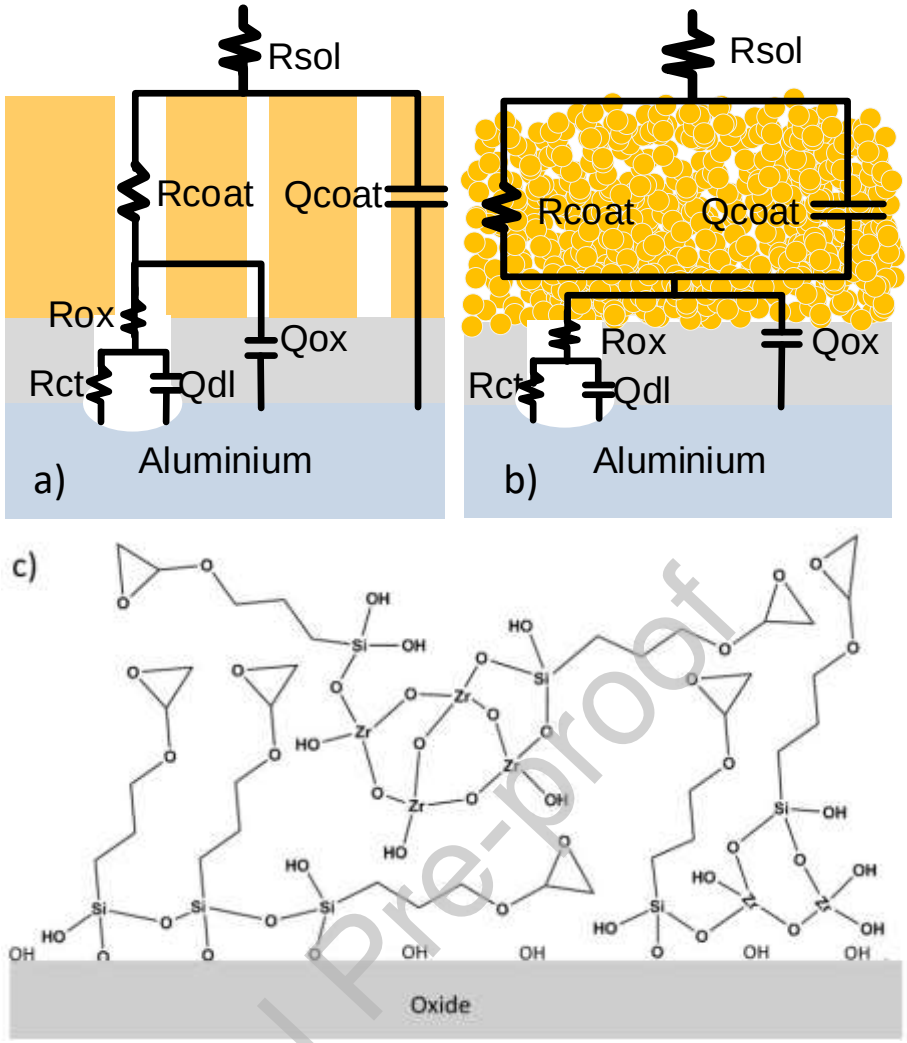

Figure 10. A scheme of two EC models with the arrangement of elements in the hierarchical model (a) and in the series combination model (b); the interface between the sol-gel and oxide (c).

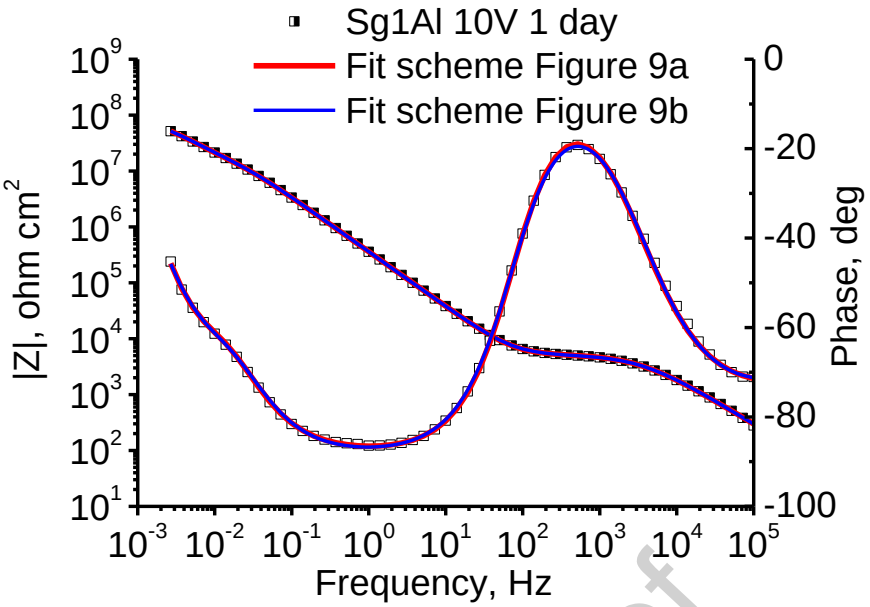

Figure 11. EIS spectrum of sample Sg1Al10V after 1 day of immersion and fit lines using EC models shown in Figure 10.

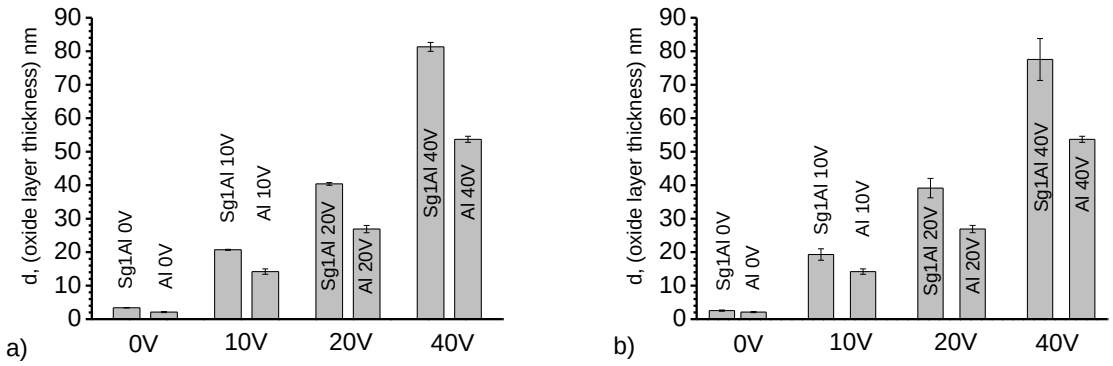

Figure 12. The calculated thickness of the aluminium oxide layer of sol-gel coated and uncoated samples; oxide thickness was obtained using equation 1 (a) and equation 2 (b).

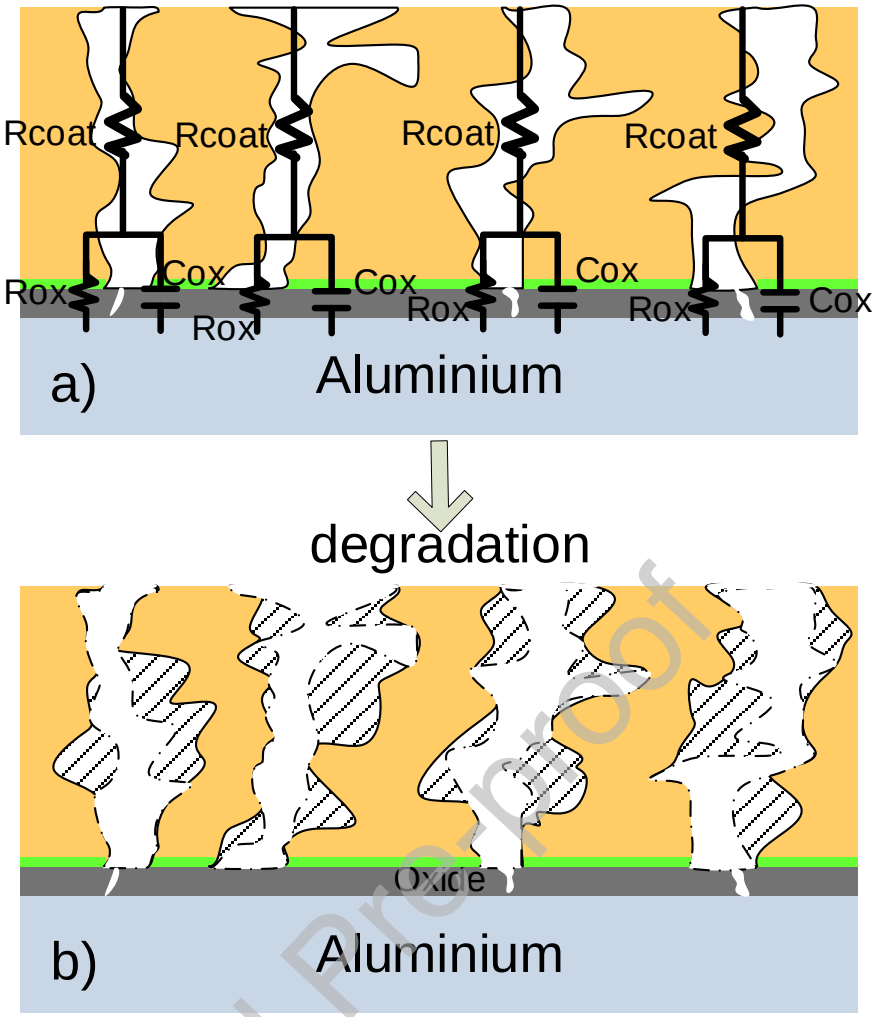

Figure 13. Degradation mechanism of the sol-gel coated anodised aluminium samples during immersion.

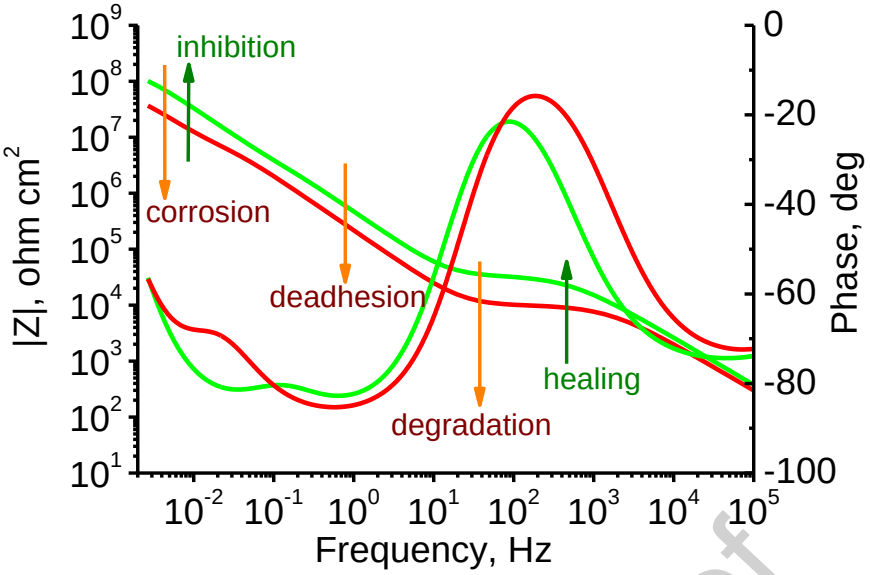

Figure 14. A schematic representation of Bode plots demonstrating the degradation/healing events in the coating, deadhesion at the oxide/coating interface and corrosion and inhibition phenomena.

Declaration of interests

☒ The authors declare that they have no known competing financial interests or personal relationships that could have appeared to influence the work reported in this paper.

☐The authors declare the following financial interests/personal relationships which may be considered as potential competing interests:

Graphical abstract